Acta Polytechnica **66**(1):1–18, 2026
https://doi.org/10.14311/AP.2026.66.0001

Published by the Czech Technical University in Prague

CALCULATING THE DYNAMIC DISTURBANCES OF WEAPON SYSTEMS ON UNMANNED GROUND VEHICLES

Viet Dung Bui[a,*], Martin Macko[a], Ba Ngoc Dang[a], Huu Nguyen Pham[b]

[a] *University of Defence in Brno, Department of Weapons and Ammunition, Kounicova 156, 662 10 Brno, Czech Republic*

[b] *Tran Dai Nghia University, Faculty of Ammunition, Department of Explosives and Ballistics, 189 Nguyen Oanh, 70000 Hochiminh, Vietnam*

[*] corresponding author: vietdung.bui@unob.cz

Abstract. This paper investigates the dynamic disturbances affecting weapon systems mounted on unmanned ground vehicles (UGVs), which pose a significant challenge in maintaining aiming accuracy when moving across uneven terrain. These disturbances arise from terrain-induced vibrations, complex hull movements, suspension-induced vibrations, and cross-inertial interactions between the gun barrel and the turret, particularly under asymmetrical road excitations. This research aims to develop a comprehensive mathematical model describing the dynamic disturbances caused by mass imbalances and cross-inertial effects in weapon-UGV systems and to analyse the influence of asymmetrical and non-uniform road surfaces on weapon system vibrations. The proposed nonlinear dynamic model is constructed using Euler rotation matrices and coordinate transformation methods, incorporating suspension-induced disturbances. An uneven road model with varying roughness heights between the left and right sides and asymmetrical profiles was introduced, including sequential semi-sinusoidal, trapezoidal, and rectangular ridge shapes to represent battlefield-like terrain conditions. The governing equations were solved in MATLAB-Simulink to evaluate weapon vibrations, angular deviations, and disturbance torques. The simulation results showed that asymmetrical road excitation significantly amplified the disturbances to the weapon system during aiming. A scaled UGV model was used to conduct experiments on vehicle body vibrations while moving over a rough terrain section, assessing the effect of suspension and uneven road surfaces on the weapon system. The results demonstrate that the developed dynamic disturbance model provides a solid basis for future stabilisation and compensation control strategies. It improves the firing accuracy of weapon systems mounted on unmanned ground vehicles operating in real-world conditions.

Keywords: Weapon system, 2-axis gimbal, dynamic disturbances, mathematical model, unmanned ground vehicle (UGV).

1. Introduction

Mathematical models of 2-axis or 3-axis gimbal systems have been widely studied and used in civil, aerospace, and defence fields. The weapon system on an UGV can also be considered as a 2-axis gimbal system. A camera is mounted on the barrel for monitoring, providing live images from the barrel's point of view, helping the automatic control system to accurately determine targets. Camera systems are often used in unmanned aircraft or guided missiles to calculate and compensate for deviations caused by the movement of the vehicle to ensure that it is always aimed at the target. During movement, the cameras are always unstable due to disturbances caused by many different factors. For autonomous vehicles, dynamic imbalance occurs when the mass of the vehicle, turret, weapon, or rotating parts is not evenly distributed, creating unwanted vibrations and interference moments. This reduces the accuracy of the weapon, affects the sensor, and causes instability when moving. In order to maintain a stable line of sight, we need to create a mathematical model that can calculate dynamic disturbances. The mathematical models proposed and studied in articles [1, 2] on a two-axis gimbal system (yaw-pitch) focus on constructing kinematic equations to describe the motion of this system. The equations of motion are derived using both the moment equation method and the Lagrange equation method, which help to determine the influence of factors such as inertia, disturbance, and the interactions between axes. The article [3] studies and proposes a cascade control system for a two-axis gimbal system with mass imbalance, aiming to stabilise the camera's line of sight in a disturbed environment. The article demonstrates that the cascade control system significantly improves the stability and performance of the two-axis gimbal system under disturbance conditions. The simulation results confirm that this system can improve line-of-sight accuracy, which is particularly important for applications such as target tracking systems, weapon guidance, and sensor stabilisation on mobile platforms. The articles [4, 5] present a two-axis gimbal stabilisation system using a self-tuning fuzzy

PID controller used to maintain the line of sight of the sensor under disturbance conditions. It derives the equation of motion using the Lagrange method and considers the influence of the angular velocity of the platform, the imbalance of dynamic mass, and the interaction between the two yaw-pitch axes. The authors built a self-tuning fuzzy PID control system and designed a stable control loop with a cross-coupler to reduce the disturbance between the axes. Their work also compares the performance of the fuzzy PID controller and the traditional PI controller. In [6], the authors focused on the development and evaluation of turret and barrel control methods on main battle tanks (MBT), and modelled the turret and barrel control system.

Previous studies focused primarily on evaluating the disturbances in 2-axis gimbal systems, but did not consider a weapon systems mounted on unmanned vehicles, nor have they assessed the influence of road surface conditions on line-of-sight stability. To address this gap, this paper develops a mathematical model of road surfaces featuring multiple bumps of varying heights and asymmetrical left-right profiles. A scaled UGV model was used to experimentally measure vehicle body vibrations while traversing the uneven terrain, allowing assessment of the effects of both the road surface and the suspension system on the weapon system. Based on these analyses, a model to calculate dynamic disturbances on the weapon system was established, providing the foundation for designing a line-of-sight stabilisation controller for weapon systems mounted on UGVs.

2. Mathematical model

2.1. Mathematical model of unmanned vehicle

This study uses a four-wheeled UGV model with front and rear axles [7–11]. The road surface profile is modelled as a sequence of semi-sinusoidal, trapezoidal, and rectangular bumps. Asymmetry is introduced by assigning different bump heights to the left and right sides of the road surface. The investigated road surface model is illustrated in Figure 1.

The excitations from the road surface profile acting on the four wheels are denoted as q_{1T}, q_{1P}, q_{2T}, q_{2P}:

$$q_{1T}=\begin{cases}0, & (0\le t<1.2\,\mathrm{s})\\ 0.1\sin[13.09(t-1.2)], & (1.2\,\mathrm{s}\le t<1.44\,\mathrm{s})\\ 0, & (1.44\,\mathrm{s}\le t<2.64\,\mathrm{s})\\ 0.05, & (t=2.64\,\mathrm{s})\\ \frac{5}{6}t-2.15, & (2.64\,\mathrm{s}<t<2.7\,\mathrm{s})\\ 0.1, & (2.7\,\mathrm{s}\le t<2.82\,\mathrm{s})\\ -\frac{5}{6}t+2.45, & (2.82\,\mathrm{s}\le t<2.88\,\mathrm{s})\\ 0.05, & (t=2.88\,\mathrm{s})\\ 0, & (2.88\,\mathrm{s}<t<4.08\,\mathrm{s})\\ 0.1, & (4.08\,\mathrm{s}\le t<4.32\,\mathrm{s})\\ 0, & (t\ge 4.32\,\mathrm{s})\end{cases} \tag{1}$$

$$q_{2T}=\begin{cases}0, & (0\le t<1.536\,\mathrm{s})\\ 0.1\sin[13.09\\ \qquad(t-1.536)], & (1.536\le t<1.776\,\mathrm{s})\\ 0, & (1.776\le t<2.976\,\mathrm{s})\\ 0.05, & (t=2.976\,\mathrm{s})\\ \frac{5}{6}t-2.43, & (2.976\,\mathrm{s}<t<3.036\,\mathrm{s})\\ 0.1, & (3.036\,\mathrm{s}\le t<3.156\,\mathrm{s})\\ -\frac{5}{6}t+2.73, & (3.156\,\mathrm{s}\le t<3.216\,\mathrm{s})\\ 0.05, & (t=3.216\,\mathrm{s})\\ 0, & (3.216\,\mathrm{s}<t<4.416\,\mathrm{s})\\ 0.1, & (4.416\,\mathrm{s}\le t<4.656\,\mathrm{s})\\ 0, & (t\ge 4.656\,\mathrm{s})\end{cases} \tag{2}$$

$$q_{1P}=\begin{cases}0, & (0\le t<1.8\,\mathrm{s})\\ 0.15, & (1.8\,\mathrm{s}\le t<1.98\,\mathrm{s})\\ 0, & (1.98\,\mathrm{s}\le t<3.18\,\mathrm{s})\\ 0.15\sin[17.45\\ \qquad(t-3.18)], & (3.18\,\mathrm{s}\le t<3.36\,\mathrm{s})\\ 0, & (3.36\,\mathrm{s}<t<4.56\,\mathrm{s})\\ 0.05, & (t=4.56\,\mathrm{s})\\ \frac{5}{3}t-7.55, & (4.56\,\mathrm{s}<t<4.62\,\mathrm{s})\\ 0.15, & (4.62\,\mathrm{s}\le t<4.68\,\mathrm{s})\\ -\frac{5}{3}t+7.95, & (4.68\,\mathrm{s}\le t<4.74\,\mathrm{s})\\ 0.05, & (t=4.74\,\mathrm{s})\\ 0, & (t>4.74\,\mathrm{s})\end{cases} \tag{3}$$

$$q_{2P}=\begin{cases}0 & (0\le t<2.136\,\mathrm{s})\\ 0.15 & (2.136\,\mathrm{s}\le t<2.316\,\mathrm{s})\\ 0 & (2.316\,\mathrm{s}\le t<3.516\,\mathrm{s})\\ 0.15\sin[17.45\\ \qquad(t-3.516)], & (3.516\le t<3.696\,\mathrm{s})\\ 0 & (3.696\le t<4.896\,\mathrm{s})\\ 0.05 & (t=4.896\,\mathrm{s})\\ \frac{5}{3}t-8.11 & (4.896\,\mathrm{s}<t<4.956\,\mathrm{s})\\ 0.15 & (4.956\,\mathrm{s}\le t<5.016\,\mathrm{s})\\ -\frac{5}{3}t+8.51 & (5.016\,\mathrm{s}\le t<5.076\,\mathrm{s})\\ 0.05 & (t=5.076\,\mathrm{s})\\ 0 & (t>5.076\,\mathrm{s})\end{cases} \tag{4}$$

The UGV model along with its geometric parameters is illustrated in Figure 2 [12, 13].

The model uses 3 coordinate systems, the $O_0X_0Y_0Z_0$ coordinate system is located at the centre of gravity of the vehicle body, the $O_1X_1Y_1Z_1$ coordinate system is located at the centre of gravity of the front axle, and the $O_2X_2Y_2Z_2$ coordinate system is located at the centre of gravity of the rear axle.

According to documents [11–15], the mathematical equation system of an unmanned ground vehicle consists of 7 equations with 7 unknowns: Z_{01}, φ_1, Z_{02},

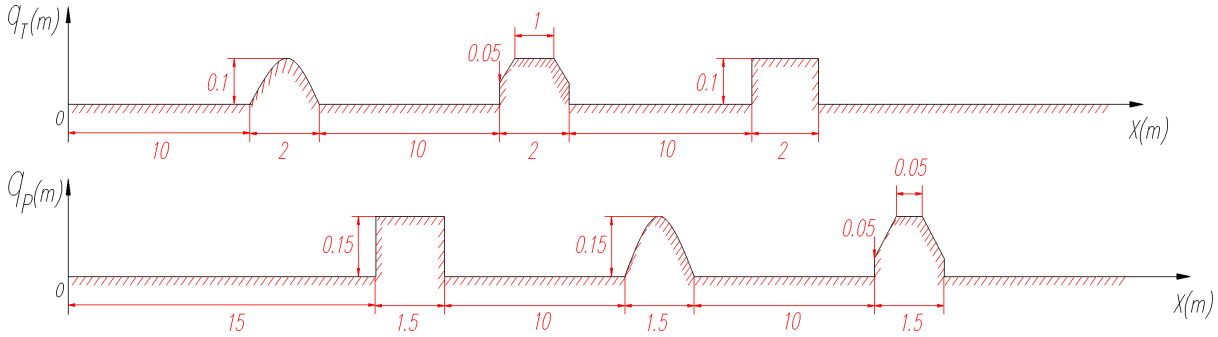

FIGURE 1. Road surface profile model.

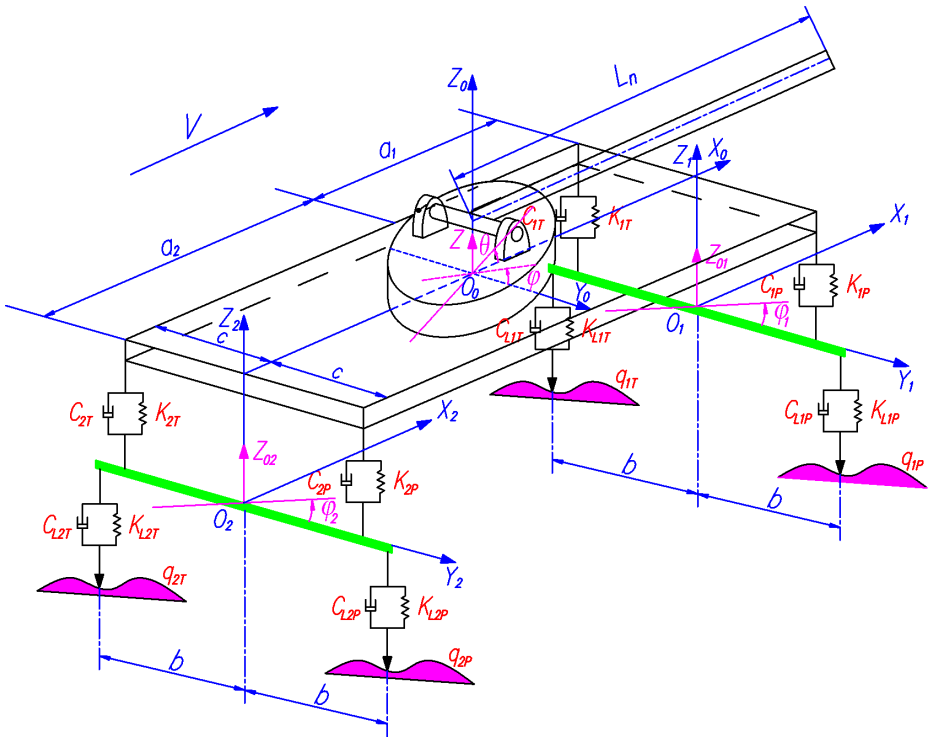

FIGURE 2. The unmanned vehicle model.

φ_2, Z, φ, θ. In which the front axle has 2 degrees of freedom, Z_{01} and φ_1, the rear axle has 2 degrees of freedom, Z_{02} and φ_2, and the vehicle body has 3 degrees of freedom, Z, φ, and θ:

$$\begin{aligned}
m_1\ddot{Z}_{01} =& -F_{CL1T} - F_{KL1T} - F_{CL1P} - F_{KL1P} \\
&+ F_{C1T} + F_{K1T} + F_{C1P} + F_{K1P}, \\
J_{m1}\ddot{\varphi}_1 =& \, b[(F_{CL1T} + F_{KL1T}) - (F_{CL1P} + F_{KL1P})] \\
&+ c[(F_{C1P} + F_{K1P}) - (F_{C1T} + F_{K1T})], \\
m_2\ddot{Z}_{02} =& -F_{CL2T} - F_{KL2T} - F_{CL2P} - F_{KL2P} \\
&+ F_{C2T} + F_{K2T} + F_{C2P} + F_{K2P}, \\
J_{m2}\ddot{\varphi}_2 =& \, b[(F_{CL2T} + F_{KL2T}) - (F_{CL2P} + F_{KL2P})] \\
&+ c[(F_{C2P} + F_{K2P}) - (F_{C2T} + F_{K2T})], \\
M\ddot{Z} =& -F_{C1T} - F_{K1T} - F_{C1P} - F_{K1P} - F_{C2T} \\
&- F_{K2T} - F_{C2P} - F_{K2P}, \\
J_\varphi\ddot{\varphi} =& \, c[(F_{C1T} + F_{K1T}) - (F_{C1P} + F_{K1P})] \\
&+ c[(F_{C2T} + F_{K2T}) - (F_{C2P} + F_{K2P})], \\
J_\theta\ddot{\theta} =& -a_1[(F_{C1P} + F_{K1P}) + (F_{C1T} + F_{K1T})] \\
&+ a_2[(F_{C2P} + F_{K2P}) + (F_{C2T} + F_{K2T})],
\end{aligned} \tag{5}$$

where:

$$\begin{aligned}
F_{KL1T} &= K_{L1T}(Z_{01} + b\varphi_1 - q_{1T}), \\
F_{CL1T} &= C_{L1T}(\dot{Z}_{01} + b\dot{\varphi}_1 - \dot{q}_{1T}), \\
F_{KL1P} &= K_{L1P}(Z_{01} - b\varphi_1 - q_{1P}), \\
F_{CL1P} &= C_{L1P}(\dot{Z}_{01} - b\dot{\varphi}_1 - \dot{q}_{1P}), \\
F_{K1T} &= K_{1T}(Z - a_1\theta + c\varphi - Z_{01} - b\varphi_1), \\
F_{C1T} &= C_{1T}(\dot{Z} - a_1\dot{\theta} + c\dot{\varphi} - \dot{Z}_{01} - b\dot{\varphi}_1), \\
F_{K1P} &= K_{1P}(Z - a_1\theta - c\varphi - Z_{01} + b\varphi_1), \\
F_{C1P} &= C_{1P}(\dot{Z} - a_1\dot{\theta} - c\dot{\varphi} - \dot{Z}_{01} + b\dot{\varphi}_1),
\end{aligned} \tag{6}$$

$$\begin{aligned}
F_{KL2T} &= K_{L2T}(Z_{02} + b\varphi_2 - q_{2T}), \\
F_{CL2T} &= C_{L2T}(\dot{Z}_{02} + b\dot{\varphi}_2 - \dot{q}_{2T}), \\
F_{KL2P} &= K_{L2P}(Z_{02} - b\varphi_2 - q_{2P}), \\
F_{CL2P} &= C_{L2P}(\dot{Z}_{02} - b\dot{\varphi}_2 - \dot{q}_{2P}), \\
F_{K2T} &= K_{2T}(Z + a_2\theta + c\varphi - Z_{02} - b\varphi_2), \\
F_{C2T} &= C_{2T}(\dot{Z} + a_2\dot{\theta} + c\dot{\varphi} - \dot{Z}_{02} - b\dot{\varphi}_2), \\
F_{K2P} &= K_{2P}(Z + a_2\theta - c\varphi - Z_{02} + b\varphi_2), \\
F_{C2P} &= C_{2P}(\dot{Z} + a_2\dot{\theta} - c\dot{\varphi} - \dot{Z}_{02} + b\dot{\varphi}_2).
\end{aligned} \tag{7}$$

By substituting the expressions for the elastic and damping forces into the system of Equations (5), we obtain the following system:

$$
\begin{aligned}
m_1\ddot{Z}_{01} &= -C_{L1T}(\dot{Z}_{01} - b\dot{\varphi}_1 - \dot{q}_{1T}) - K_{L1T}(Z_{01} - b\varphi_1 - q_{1T}) \\
&\quad - C_{L1P}(\dot{Z}_{01} + b\dot{\varphi}_1 - \dot{q}_{1P}) - K_{L1P}(Z_{01} + b\varphi_1 - q_{1P}) \\
&\quad + C_{1T}(\dot{Z} + a_1\dot{\theta} - c\dot{\varphi} - \dot{Z}_{01} + b\dot{\varphi}_1) \\
&\quad + K_{1T}(Z + a_1\theta - c\varphi - Z_{01} + b\varphi_1) \\
&\quad + C_{1P}(\dot{Z} + a_1\dot{\theta} + c\dot{\varphi} - \dot{Z}_{01} - b\dot{\varphi}_1) \\
&\quad + K_{1P}(Z + a_1\theta + c\varphi - Z_{01} - b\varphi_1), \\
J_{m1}\ddot{\varphi}_1 &= b[C_{L1T}(\dot{Z}_{01} - b\dot{\varphi}_1 - \dot{q}_{1T}) + K_{L1T}(Z_{01} - b\varphi_1 - q_{1T}) \\
&\quad - C_{L1P}(\dot{Z}_{01} + b\dot{\varphi}_1 - \dot{q}_{1P}) - K_{L1P}(Z_{01} + b\varphi_1 - q_{1P})] \\
&\quad + c[C_{1P}(\dot{Z} + a_1\dot{\theta} + c\dot{\varphi} - \dot{Z}_{01} - b\dot{\varphi}_1) \\
&\quad + K_{1P}(Z + a_1\theta + c\varphi - Z_{01} - b\varphi_1) \\
&\quad - C_{1T}(\dot{Z} + a_1\dot{\theta} - c\dot{\varphi} - \dot{Z}_{01} + b\dot{\varphi}_1) \\
&\quad - K_{1T}(Z + a_1\theta - c\varphi - Z_{01} + b\varphi_1)], \\
m_2\ddot{Z}_{02} &= -C_{L2T}(\dot{Z}_{02} - b\dot{\varphi}_2 - \dot{q}_{2T}) - K_{L2T}(Z_{02} - b\varphi_2 - q_{2T}) \\
&\quad - C_{L2P}(\dot{Z}_{02} + b\dot{\varphi}_2 - \dot{q}_{2P}) - K_{L2P}(Z_{02} + b\varphi_2 - q_{2P}) \\
&\quad + C_{2T}(\dot{Z} - a_2\dot{\theta} - c\dot{\varphi} - \dot{Z}_{02} + b\dot{\varphi}_2) \\
&\quad + K_{2T}(Z - a_2\theta - c\varphi - Z_{02} + b\varphi_2) \\
&\quad + C_{2P}(\dot{Z} - a_2\dot{\theta} + c\dot{\varphi} - \dot{Z}_{02} - b\dot{\varphi}_2) \\
&\quad + K_{2P}(Z - a_2\theta + c\varphi - Z_{02} - b\varphi_2), \\
J_{m2}\ddot{\varphi}_2 &= b[C_{L2T}(\dot{Z}_{02} - b\dot{\varphi}_2 - \dot{q}_{2T}) + K_{L2T}(Z_{02} - b\varphi_2 - q_{2T}) \\
&\quad - C_{L2P}(\dot{Z}_{02} + b\dot{\varphi}_2 - \dot{q}_{2P}) - K_{L2P}(Z_{02} + b\varphi_2 - q_{2P})] \\
&\quad + c[C_{2P}(\dot{Z} - a_2\dot{\theta} + c\dot{\varphi} - \dot{Z}_{02} - b\dot{\varphi}_2) \\
&\quad + K_{2P}(Z - a_2\theta + c\varphi - Z_{02} - b\varphi_2) \\
&\quad - C_{2T}(\dot{Z} - a_2\dot{\theta} - c\dot{\varphi} - \dot{Z}_{02} + b\dot{\varphi}_2) \\
&\quad - K_{2T}(Z - a_2\theta - c\varphi - Z_{02} + b\varphi_2)], \\
M\ddot{Z} &= -C_{1T}(\dot{Z} + a_1\dot{\theta} - c\dot{\varphi} - \dot{Z}_{01} + b\dot{\varphi}_1) \\
&\quad - K_{1T}(Z + a_1\theta - c\varphi - Z_{01} + b\varphi_1) \\
&\quad - C_{1P}(\dot{Z} + a_1\dot{\theta} + c\dot{\varphi} - \dot{Z}_{01} - b\dot{\varphi}_1) \\
&\quad - K_{1P}(Z + a_1\theta + c\varphi - Z_{01} - b\varphi_1) \\
&\quad - C_{2T}(\dot{Z} - a_2\dot{\theta} - c\dot{\varphi} - \dot{Z}_{02} + b\dot{\varphi}_2) \\
&\quad - K_{2T}(Z - a_2\theta - c\varphi - Z_{02} + b\varphi_2) \\
&\quad - C_{2P}(\dot{Z} - a_2\dot{\theta} + c\dot{\varphi} - \dot{Z}_{02} - b\dot{\varphi}_2) \\
&\quad - K_{2P}(Z - a_2\theta + c\varphi - Z_{02} - b\varphi_2), \\
J_x\ddot{\varphi} &= c[C_{1T}(\dot{Z} + a_1\dot{\theta} - c\dot{\varphi} - \dot{Z}_{01} + b\dot{\varphi}_1) \\
&\quad + K_{1T}(Z + a_1\theta - c\varphi - Z_{01} + b\varphi_1) \\
&\quad - C_{1P}(\dot{Z} + a_1\dot{\theta} + c\dot{\varphi} - \dot{Z}_{01} - b\dot{\varphi}_1) \\
&\quad - K_{1P}(Z + a_1\theta + c\varphi - Z_{01} - b\varphi_1)] \\
&\quad + c[C_{2T}(\dot{Z} - a_2\dot{\theta} - c\dot{\varphi} - \dot{Z}_{02} + b\dot{\varphi}_2) \\
&\quad + K_{2T}(Z - a_2\theta - c\varphi - Z_{02} + b\varphi_2) \\
&\quad - C_{2P}(\dot{Z} - a_2\dot{\theta} + c\dot{\varphi} - \dot{Z}_{02} - b\dot{\varphi}_2) \\
&\quad - K_{2P}(Z - a_2\theta + c\varphi - Z_{02} - b\varphi_2)], \\
J_y\ddot{\theta} &= -a_1[C_{1P}(\dot{Z} + a_1\dot{\theta} + c\dot{\varphi} - \dot{Z}_{01} - b\dot{\varphi}_1) \\
&\quad + K_{1P}(Z + a_1\theta + c\varphi - Z_{01} - b\varphi_1) \\
&\quad + C_{1T}(\dot{Z} + a_1\dot{\theta} - c\dot{\varphi} - \dot{Z}_{01} + b\dot{\varphi}_1) \\
&\quad + K_{1T}(Z + a_1\theta - c\varphi - Z_{01} + b\varphi_1)] \\
&\quad + a_2[C_{2P}(\dot{Z} - a_2\dot{\theta} + c\dot{\varphi} - \dot{Z}_{02} - b\dot{\varphi}_2) \\
&\quad + K_{2P}(Z - a_2\theta + c\varphi - Z_{02} - b\varphi_2) \\
&\quad + C_{2T}(\dot{Z} - a_2\dot{\theta} - c\dot{\varphi} - \dot{Z}_{02} + b\dot{\varphi}_2) \\
&\quad + K_{2T}(Z - a_2\theta - c\varphi - Z_{02} + b\varphi_2)].
\end{aligned}
\tag{8}
$$

2.2. Computational model of kinetic disturbance of weapon system

The article uses the following coordinate systems for the model [2, 3, 16, 17]:

In Figure 3, $Oxyz$ is the coordinate system attached to the vehicle body, $Amnz$ is the coordinate system attached to the turret's rotation axis, $Bpnq$ is the coordinate system located at the axis of rotation of the barrel. The p axis coincides with that of the camera. The turret rotates at an angle γ in the horizontal plane, the barrel rotates at an angle ε in the vertical plane.

We have the following reference system transformation matrices of rotation angles γ, ε:

$$
\begin{aligned}
{}^{A}_{O}M &= \begin{bmatrix} \cos\gamma & \sin\gamma & 0 \\ -\sin\gamma & \cos\gamma & 0 \\ 0 & 0 & 1 \end{bmatrix}, \\
{}^{B}_{A}M &= \begin{bmatrix} \cos\varepsilon & 0 & -\sin\varepsilon \\ 0 & 1 & 0 \\ \sin\varepsilon & 0 & \cos\varepsilon \end{bmatrix},
\end{aligned}
\tag{9}
$$

where ${}^{A}_{O}M$, ${}^{B}_{A}M$ are the basis transformation matrices from the $Amnz$ to $Oxyz$ axis system and from the $Bpnq$ to $Amnz$ axis system, respectively. The inertial angular velocity vectors of the vehicle body, turret, and barrel are determined as follows:

$$
\vec{\omega}_O = \begin{bmatrix} \omega_{Ox} \\ \omega_{Oy} \\ \omega_{Oz} \end{bmatrix}, \quad \vec{\omega}_A = \begin{bmatrix} \omega_{Am} \\ \omega_{An} \\ \omega_{Az} \end{bmatrix}, \quad \vec{\omega}_B = \begin{bmatrix} \omega_{Bp} \\ \omega_{Bn} \\ \omega_{Bq} \end{bmatrix}, \tag{10}
$$

where ω_{Ox}, ω_{Oy}, and ω_{Oz} are the angular velocity components of the vehicle body in inertial space around the x, y, and z axes, ω_{Am}, ω_{An}, and ω_{Az} are the angular velocity components of the turret in inertial space around the m, n, and z axes, ω_{Bp}, ω_{Bn}, and ω_{Bq} are the angular velocity components of the barrel in inertial space around the p, n, and q axes. According to the settings in Section 2.1: $\omega_{Ox} = \dot{\theta}$, $\omega_{Oy} = \dot{\varphi}$, $\omega_{Oz} = 0$.

The inertial mass matrix of the turret and the barrel is defined as follows:

$$
\begin{aligned}
I_A &= \begin{bmatrix} A_m & A_{mn} & A_{mz} \\ A_{mn} & A_n & A_{nz} \\ A_{mz} & A_{nz} & A_z \end{bmatrix}, \\
I_B &= \begin{bmatrix} B_p & B_{pn} & B_{pq} \\ B_{pn} & B_n & B_{nq} \\ B_{pq} & B_{nq} & B_q \end{bmatrix}.
\end{aligned}
\tag{11}
$$

The transformation of angular velocity between the reference systems is as follows:

$$
\begin{aligned}
\omega_{Am} &= \omega_{Ox}\cos\gamma + \omega_{Oy}\sin\gamma, \\
\omega_{An} &= -\omega_{Ox}\sin\gamma + \omega_{Oy}\cos\gamma, \\
\omega_{Az} &= \omega_{Oz} + \dot{\gamma},
\end{aligned}
\tag{12}
$$

$$
\begin{aligned}
\omega_{Bp} &= \omega_{Am}\cos\varepsilon - \omega_{Az}\sin\varepsilon, \\
\omega_{Bn} &= \omega_{An} + \dot{\varepsilon}, \\
\omega_{Bq} &= \omega_{Am}\sin\varepsilon + \omega_{Az}\cos\varepsilon.
\end{aligned}
\tag{13}
$$

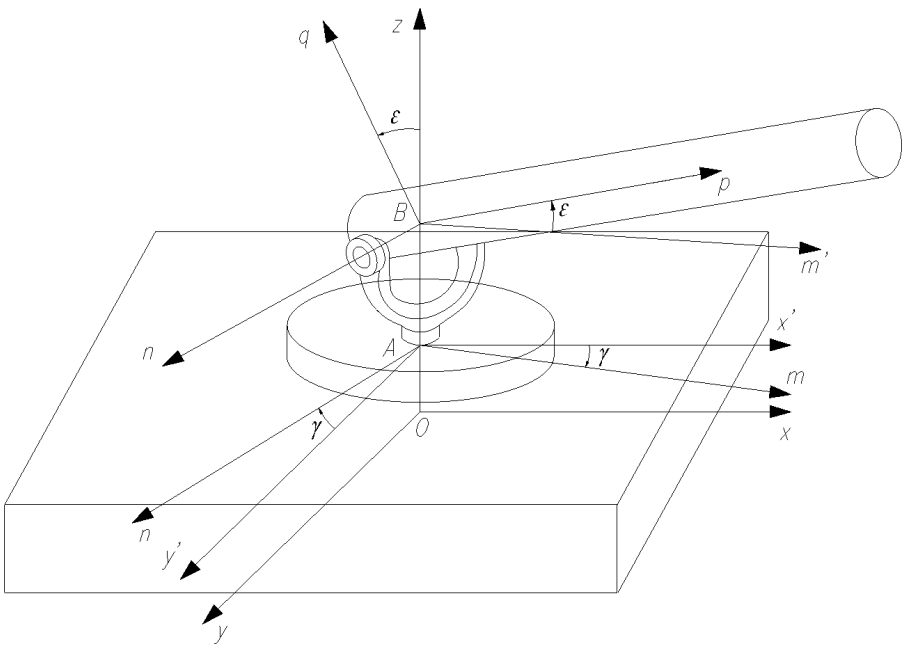

FIGURE 3. Computational model of dynamic disturbance of weapon system on unmanned vehicle.

The orientation of the weapon system on the unmanned vehicle is determined by four independent consecutive rotation angles φ_E, θ_E, ψ, and ε. Where φ_E, θ_E, and ψ are the Euler rotation angles of the turret and ε is the rotation angle of the barrel.

The kinetic energy of the weapon system is determined by the formula $T = T_1 + T_2$, where T_1 is the rotational kinetic energy of the turret and T_2 is the rotational kinetic energy of the barrel:

$$\begin{aligned} T_1 &= \frac{1}{2}\vec{\omega}_A^T I_A \vec{\omega}_A \\ &= \frac{1}{2}\begin{bmatrix}\omega_{Am} & \omega_{An} & \omega_{Az}\end{bmatrix}\begin{bmatrix}A_m & A_{mn} & A_{mz} \\ A_{mn} & A_n & A_{nz} \\ A_{mz} & A_{nz} & A_z\end{bmatrix}\begin{bmatrix}\omega_{Am} \\ \omega_{An} \\ \omega_{Az}\end{bmatrix} \\ &= \frac{1}{2}\left(A_m\omega_{Am}^2 + A_n\omega_{An}^2 + A_z\omega_{Az}^2\right) + A_{mn}\omega_{Am}\omega_{An} \\ &\quad + A_{mz}\omega_{Az}\omega_{Am} + A_{nz}\omega_{An}\omega_{Az}, \end{aligned} \tag{14}$$

$$\begin{aligned} T_2 &= \frac{1}{2}\vec{\omega}_B^T I_B \vec{\omega}_B \\ &= \frac{1}{2}\begin{bmatrix}\omega_{Bp} & \omega_{Bn} & \omega_{Bq}\end{bmatrix}\begin{bmatrix}B_p & B_{pn} & B_{pq} \\ B_{pn} & B_n & B_{nq} \\ B_{pq} & B_{nq} & B_q\end{bmatrix}\begin{bmatrix}\omega_{Bp} \\ \omega_{Bn} \\ \omega_{Bq}\end{bmatrix} \\ &= \frac{1}{2}\left(B_p\omega_{Bp}^2 + B_n\omega_{Bn}^2 + B_q\omega_{Bq}^2\right) + B_{pn}\omega_{Bp}\omega_{Bn} \\ &\quad + B_{pq}\omega_{Bq}\omega_{Bp} + B_{nq}\omega_{Bn}\omega_{Bq}, \end{aligned} \tag{15}$$

$$\begin{aligned} T = &\frac{1}{2}\left(A_m\omega_{Am}^2 + A_n\omega_{An}^2 + A_z\omega_{Az}^2\right) + A_{mn}\omega_{Am}\omega_{An} \\ &+ A_{mz}\omega_{Az}\omega_{Am} + A_{nz}\omega_{An}\omega_{Az} \\ &+ \frac{1}{2}\left(B_p\omega_{Bp}^2 + B_n\omega_{Bn}^2 + B_q\omega_{Bq}^2\right) + B_{pn}\omega_{Bp}\omega_{Bn} \\ &+ B_{pq}\omega_{Bq}\omega_{Bp} + B_{nq}\omega_{Bn}\omega_{Bq}. \end{aligned} \tag{16}$$

The Euler system determines the rotational motion of the turret by 3 rotation angles, φ_E, θ_E, and ψ, around 3 coordinate axes, then the angular velocities of the turret are determined in the Euler system as follows:

$$\begin{aligned} \omega_{Am} &= \dot{\varphi}_E \cos\theta_E \cos\psi + \dot{\theta}_E \sin\psi, \\ \omega_{An} &= -\dot{\varphi}_E \cos\theta_E \sin\psi + \dot{\theta}_E \cos\psi, \\ \omega_{Az} &= \dot{\varphi}_E \sin\theta_E + \dot{\psi}. \end{aligned} \tag{17}$$

2.2.1. Mathematical equation system of the turret

According to [3–5], by applying Lagrange's equation to the motion of the turret around the turning angle ψ, we obtain:

$$\frac{d}{dt}\left(\frac{\partial T}{\partial \dot{\psi}}\right) - \frac{\partial T}{\partial \psi} = T_A. \tag{18}$$

From Equations (17) and (13), we can calculate the partial derivatives of the angular velocities with respect to $\dot{\psi}$ and ψ:

$$\begin{aligned} \frac{\partial \omega_{Am}}{\partial \dot{\psi}} &= 0, \\ \frac{\partial \omega_{An}}{\partial \dot{\psi}} &= 0, \\ \frac{\partial \omega_{Az}}{\partial \dot{\psi}} &= 1, \\ \frac{\partial \omega_{Am}}{\partial \psi} &= -\dot{\varphi}_E \cos\theta_E \sin\psi + \dot{\theta}_E \cos\psi \\ &= \omega_{An}, \\ \frac{\partial \omega_{An}}{\partial \psi} &= -\dot{\varphi}_E \cos\theta_E \cos\psi - \dot{\theta}_E \sin\psi \\ &= -\omega_{Am}, \\ \frac{\partial \omega_{Az}}{\partial \psi} &= 0, \end{aligned} \tag{19}$$

$$\begin{aligned}
\frac{\partial\omega_{Bp}}{\partial\dot{\psi}} &= \frac{\partial\left(\omega_{Am}\cos\varepsilon-\omega_{Az}\sin\varepsilon\right)}{\partial\dot{\psi}} = -\sin\varepsilon,\\
\frac{\partial\omega_{Bn}}{\partial\dot{\psi}} &= \frac{\partial\left(\omega_{An}+\dot{\varepsilon}\right)}{\partial\dot{\psi}} = 0,\\
\frac{\partial\omega_{Bq}}{\partial\dot{\psi}} &= \frac{\partial\left(\omega_{Am}\sin\varepsilon+\omega_{Az}\cos\varepsilon\right)}{\partial\dot{\psi}} = \cos\varepsilon,\\
\frac{\partial\omega_{Bp}}{\partial\psi} &= \frac{\partial\left(\omega_{Am}\cos\varepsilon-\omega_{Az}\sin\varepsilon\right)}{\partial\psi} = \omega_{An}\cos\varepsilon,\\
\frac{\partial\omega_{Bn}}{\partial\psi} &= \frac{\partial\left(\omega_{An}+\dot{\varepsilon}\right)}{\partial\psi} = -\omega_{Am},\\
\frac{\partial\omega_{Bq}}{\partial\psi} &= \frac{\partial\left(\omega_{Am}\sin\varepsilon+\omega_{Az}\cos\varepsilon\right)}{\partial\psi} = \omega_{An}\sin\varepsilon.
\end{aligned} \tag{20}$$

Then, we calculate the partial derivative of kinetic energy according to $\dot{\psi}$ and ψ:

$$\begin{aligned}
\frac{\partial T}{\partial\dot{\psi}} =& -\left(B_p\omega_{Bp}+B_{pn}\omega_{Bn}+B_{pq}\omega_{Bq}\right)\sin\varepsilon\\
&+\left(B_{pq}\omega_{Bp}+B_{nq}\omega_{Bn}+B_q\omega_{Bq}\right)\cos\varepsilon\\
&+A_{mz}\omega_{Am}+A_{nz}\omega_{An}+A_z\omega_{Az},\\
\frac{\partial T}{\partial\psi} =& -\omega_{Am}\left(A_{mn}\omega_{Am}+A_n\omega_{An}+A_{nz}\omega_{Az}\right.\\
&\left.+B_{pn}\omega_{Bp}+B_n\omega_{Bn}+B_{nq}\omega_{Bq}\right)\\
&+\omega_{An}\left(A_m\omega_{Am}+A_{mn}\omega_{An}+A_{nz}\omega_{Az}\right)\\
&+\omega_{An}\left(B_p\omega_{Bp}+B_{pn}\omega_{Bn}+B_{pq}\omega_{Bq}\right)\cos\varepsilon\\
&+\omega_{An}\left(B_{pq}\omega_{Bq}+B_{nq}\omega_{Bn}+B_q\omega_{Bq}\right)\sin\varepsilon,
\end{aligned} \tag{21}$$

$$\begin{aligned}
\frac{d}{dt}\left(\frac{\partial T}{\partial\dot{\psi}}\right) =& -\left[\frac{d}{dt}(B_p\omega_{Bp}+B_{pn}\omega_{Bn}+B_{pq}\omega_{Bq})\sin\varepsilon\right.\\
&\left.+\left(B_p\omega_{Bp}+B_{pn}\omega_{Bn}+B_{pq}\omega_{Bq}\right)\dot{\varepsilon}\cos\varepsilon\right]\\
&+\frac{d}{dt}(B_{pq}\omega_{Bp}+B_{nq}\omega_{Bn}+B_q\omega_{Bq})\cos\varepsilon\\
&-(B_{pq}\omega_{Bp}+B_{nq}\omega_{Bn}+B_q\omega_{Bq})\dot{\varepsilon}\sin\varepsilon\\
&+A_{mz}\dot{\omega}_{Am}+A_{nz}\dot{\omega}_{An}+A_z\dot{\omega}_{Az},
\end{aligned} \tag{22}$$

where:

$$\begin{aligned}
\frac{d\omega_{Bp}}{dt} &= \dot{\omega}_{Am}\cos\varepsilon-\omega_{Am}\dot{\varepsilon}\sin\varepsilon\\
&\quad-\dot{\omega}_{Az}\sin\varepsilon-\omega_{Az}\dot{\varepsilon}\cos\varepsilon,\\
\frac{d\omega_{Bn}}{dt} &= \dot{\omega}_{An}+\ddot{\varepsilon},\\
\frac{d\omega_{Bq}}{dt} &= \dot{\omega}_{Am}\sin\varepsilon+\omega_{Am}\dot{\varepsilon}\cos\varepsilon\\
&\quad+\dot{\omega}_{Az}\cos\varepsilon-\omega_{Az}\dot{\varepsilon}\sin\varepsilon.
\end{aligned} \tag{23}$$

Substituting the previously derived expressions into Equation (17) yields the following result:

$$J_{Az}\dot{\omega}_{Az} = T_A+T_{da1}+T_{da2}+T_{da3}, \tag{24}$$

where:

$$\begin{aligned}
J_{Az} &= A_z+B_p\sin^2\varepsilon+B_q\cos^2\varepsilon-B_{pq}\sin(2\varepsilon),\\
T_{da1} &= \left[A_m+B_p\cos^2\varepsilon+B_q\sin^2\varepsilon+B_{pq}\sin(2\varepsilon)\right.\\
&\quad\left.-(A_n+B_n)\right]\omega_{Am}\omega_{An},\\
T_{da2} &= -\left[A_{mz}+(B_q-B_p)\sin\varepsilon\cos\varepsilon\right.\\
&\quad\left.+B_{pq}\cos(2\varepsilon)\right](\dot{\omega}_{Am}-\omega_{An}\omega_{Az})-(A_{nz}\\
&\quad+B_{nq}\cos\varepsilon-B_{pn}\sin\varepsilon)(\dot{\omega}_{An}+\omega_{Am}\omega_{Az})\\
&\quad-(A_{mn}+B_{pn}\cos\varepsilon+B_{nq}\sin\varepsilon)\\
&\quad\left(\omega_{Am}^2-\omega_{An}^2\right),\\
T_{da3} &= \ddot{\varepsilon}\left(B_{pn}\sin\varepsilon-B_{nq}\cos\varepsilon\right)+\dot{\varepsilon}\left[(B_p-B_q)\right.\\
&\quad(\omega_{Am}\cos(2\varepsilon)-\omega_{Az}\sin(2\varepsilon))\\
&\quad+2B_{pq}\left(\omega_{Am}\sin(2\varepsilon)+\omega_{Az}\cos(2\varepsilon)\right)\\
&\quad+\left(B_{nq}\sin\varepsilon+B_{pn}cos\varepsilon\right)(\omega_{An}+\omega_{Bn})\\
&\quad\left.-B_n\omega_{Am}\right],
\end{aligned} \tag{25}$$

where T_{da1} is the disturbance caused by the main moment of inertia, T_{da2} is the disturbance caused by the cross inertia components and the interaction between the axes, T_{da3} is the disturbance caused by the movement of the barrel and the angular velocity of the vehicle body.

$T_{da} = T_{da1}+T_{da2}+T_{da3}$ is the moment of inertia acting on the turret motion.

From Equation (13), we obtain:

$$\begin{aligned}
\omega_{Az} &= \frac{\omega_{Bq}-\omega_{Am}\sin\varepsilon}{\cos\varepsilon}\\
\Rightarrow\dot{\omega}_{Az} &= \frac{\dot{\omega}_{Bq}-\dot{\omega}_{Am}\sin\varepsilon-\omega_{Am}\dot{\varepsilon}\cos\varepsilon+\omega_{Az}\dot{\varepsilon}\sin\varepsilon}{\cos\varepsilon}.
\end{aligned} \tag{26}$$

Equation (24) is rewritten as follows:

$$\begin{aligned}
J_{Az}\dot{\omega}_{Bq} &= T_A\cos\varepsilon+T_{da}\cos\varepsilon+T_{da}^*,\\
T_{da}^* &= J_{Az}\left[\dot{\omega}_{Am}\sin\varepsilon+\omega_{Bp}\left(\omega_{Bn}-\omega_{An}\right)\right].
\end{aligned} \tag{27}$$

$T_{DA} = T_{da}cos\varepsilon+T_{da}^*$ is the sum of the disturbances caused by the motion of the turret in the horizontal plane:

$$\begin{aligned}
T_{da} &= T_{da1}+T_{da2}+T_{da3} = T_{B-Az}+T_{C-Az},\\
T_{B-Az} &= T_{da1}+T_{da2}+\left[(B_p-B_q)\cos(2\varepsilon)\right.\\
&\quad\left.+2B_{pq}\sin(2\varepsilon)-B_n\right]\dot{\varepsilon}\omega_{Am}\\
&\quad+\left[(B_p-B_q)\sin(2\varepsilon)\right.\\
&\quad\left.-2B_{pq}\cos(2\varepsilon)\right]\omega_{An}\omega_{Az}\\
&\quad+\left(B_{nq}\cos\varepsilon-B_{pn}\sin\varepsilon\right)\dot{\omega}_{An}\\
&\quad-\left(B_{nq}\sin\varepsilon+B_{pn}\cos\varepsilon\right)\omega_{An}^2,\\
T_{C-Az} &= \left(B_{pn}\sin\varepsilon-B_{nq}\cos\varepsilon\right)\dot{\omega}_{Bn}\\
&\quad+\left(B_{pn}\cos\varepsilon+B_{nq}\sin\varepsilon\right)\omega_{Bn}^2\\
&\quad+\left[(B_q-B_p)\sin(2\varepsilon)\right.\\
&\quad\left.+2B_{pq}\cos(2\varepsilon)\right]\omega_{Bn}\omega_{Az}.
\end{aligned} \tag{28}$$

Looking at Equation (28), T_{B-Az} is the disturbance caused by the main moment of inertia and depends on the magnitude of the angular velocity of the vehicle body, causing a direct impact on the dynamics of the turret. T_{C-Az} is the cross-disturbance moment between the turret and the barrel. It shows the influence of the barrel movement on the turret even when there is no disturbance from the vehicle body.

2.2.2. Mathematical equation system of the barrel

According to [2, 3], by applying Lagrange's equation to the motion of the barrel around the turning angle ε, we obtain:

$$\frac{d}{dt}\left(\frac{\partial T}{\partial \dot{\varepsilon}}\right) - \frac{\partial T}{\partial \varepsilon} = T_E. \tag{29}$$

From Equation (13) we can derive the partial derivatives of ω_{Bp}, ω_{Bn}, and ω_{Bq} with respect to ε, $\dot{\varepsilon}$ as follows:

$$\begin{aligned}
\frac{\partial \omega_{Bp}}{\partial \dot{\varepsilon}} &= 0,\\
\frac{\partial \omega_{Bn}}{\partial \dot{\varepsilon}} &= 1,\\
\frac{\partial \omega_{Bq}}{\partial \dot{\varepsilon}} &= 0,\\
\frac{\partial \omega_{Bp}}{\partial \varepsilon} &= -\omega_{Am}\sin\varepsilon - \omega_{Az}\cos\varepsilon\\
&= -\omega_{Bq},\\
\frac{\partial \omega_{Bn}}{\partial \varepsilon} &= 0,\\
\frac{\partial \omega_{Bq}}{\partial \varepsilon} &= \omega_{Am}\cos\varepsilon - \omega_{Az}\sin\varepsilon\\
&= \omega_{Bp}.
\end{aligned} \tag{30}$$

Kinetic energy partial derivative with respect to ε, $\dot{\varepsilon}$:

$$\begin{aligned}
\frac{\partial T}{\partial \dot{\varepsilon}} &= B_n\omega_{Bn} + B_{pn}\omega_{Bp} + B_{nq}\omega_{Bq},\\
\frac{\partial T}{\partial \varepsilon} &= \omega_{Bq}\omega_{Bp}\left(B_q - B_p\right) - B_{pn}\omega_{Bq}\omega_{Bn}\\
&\quad + B_{pq}\left(\omega_{Bp}^2 - \omega_{Bq}^2\right) + B_{nq}\omega_{Bp}\omega_{Bn},\\
\frac{d}{dt}\left(\frac{\partial T}{\partial \dot{\varepsilon}}\right) &= B_n\dot{\omega}_{Bn} + B_{pn}\dot{\omega}_{Bp} + B_{nq}\dot{\omega}_{Bq}.
\end{aligned} \tag{31}$$

Substituting Equation (30) into Equations (28) gives:

$$\begin{aligned}
&B_n\dot{\omega}_{Bn} + B_{pn}\dot{\omega}_{Bp} + B_{nq}\dot{\omega}_{Bq}\\
&\quad - \omega_{Bq}\omega_{Bp}(B_q - B_p) + B_{pn}\omega_{Bq}\omega_{Bn}\\
&\quad - B_{pq}(\omega_{Bp}^2 - \omega_{Bq}^2) - B_{nq}\omega_{Bp}\omega_{Bn} = T_E,
\end{aligned} \tag{32}$$

$$\begin{aligned}
B_n\dot{\omega}_{Bn} &= T_E + (B_q - B_p)\omega_{Bq}\omega_{Bp}\\
&\quad - B_{pn}(\dot{\omega}_{Bp} + \omega_{Bq}\omega_{Bn})\\
&\quad + B_{pq}(\omega_{Bp}^2 - \omega_{Bq}^2)\\
&\quad - B_{nq}(\dot{\omega}_{Bq} - \omega_{Bp}\omega_{Bn}),
\end{aligned} \tag{33}$$

$$\begin{aligned}
T_{DE} = (B_q - B_p)\omega_{Bq}\omega_{Bp} - B_{pn}(\dot{\omega}_{Bp} + \omega_{Bq}\omega_{Bn})\\
+ B_{pq}(\omega_{Bp}^2 - \omega_{Bq}^2) - B_{nq}(\dot{\omega}_{Bq} - \omega_{Bp}\omega_{Bn}),
\end{aligned} \tag{34}$$

where T_{DE} is the disturbance moment caused by the motion of the barrel:

$$\begin{aligned}
\omega_{Bp}\omega_{Bq} &= \frac{1}{2}(\omega_{Am}^2 - \omega_{Az}^2)\sin(2\varepsilon)\\
&\quad + \omega_{Am}\omega_{Az}\cos(2\varepsilon),\\
\omega_{Bp}^2 - \omega_{Bq}^2 &= (\omega_{Am}^2 - \omega_{Az}^2)\cos(2\varepsilon)\\
&\quad - 2\omega_{Am}\omega_{Az}\sin(2\varepsilon),\\
\dot{\omega}_{Bq} - \omega_{Bp}\omega_{Bn} &= \dot{\omega}_{Am}\sin\varepsilon + \dot{\omega}_{Az}\cos\varepsilon\\
&\quad - \omega_{Am}\omega_{An}\cos\varepsilon + \omega_{An}\omega_{Az}\sin\varepsilon,\\
\dot{\omega}_{Bp} + \omega_{Bq}\omega_{Bn} &= \dot{\omega}_{Am}\cos\varepsilon + \omega_{Am}\omega_{An}\sin\varepsilon\\
&\quad - \dot{\omega}_{Az}\sin\varepsilon + \omega_{An}\omega_{Az}\cos\varepsilon.
\end{aligned} \tag{35}$$

Substituting Equation (34) into T_{DE} gives:

$$\begin{aligned}
T_{DE} = &-(B_{nq}\sin\varepsilon + B_{pn}\cos\varepsilon)(\dot{\omega}_{Am} + \omega_{An}\omega_{Az})\\
&+ (B_{nq}\cos\varepsilon + B_{pn}\sin\varepsilon)\omega_{Am}\omega_{An}\\
&+ [(B_q - B_p)\cos(2\varepsilon) - 2B_{pq}\sin(2\varepsilon)]\,\omega_{Am}\omega_{Az}\\
&+ \frac{1}{2}[(B_q - B_p)\sin(2\varepsilon) + 2B_{pq}\cos(2\varepsilon)]\,\omega_{Am}^2\\
&+ (B_{pn}\sin\varepsilon - B_{nq}\cos\varepsilon)\dot{\omega}_{Az}\\
&- \frac{1}{2}[(B_q - B_p)\sin(2\varepsilon) + 2B_{pn}\cos(2\varepsilon)]\,\omega_{Az}^2,\\
T_{DE} = &\ T_{BE} + T_{CE},
\end{aligned} \tag{36}$$

$$\begin{aligned}
T_{BE} = &-(B_{nq}\sin\varepsilon + B_{pn}\cos\varepsilon)(\dot{\omega}_{Am} + \omega_{An}\omega_{Az})\\
&+ (B_{nq}\cos\varepsilon + B_{pn}\sin\varepsilon)\omega_{Am}\omega_{An}\\
&+ [(B_q - B_p)\cos(2\varepsilon) - 2B_{pq}\sin(2\varepsilon)]\,\omega_{Am}\omega_{Az}\\
&+ \frac{1}{2}[(B_q - B_p)\sin(2\varepsilon) + 2B_{pq}\cos(2\varepsilon)]\,\omega_{Am}^2,\\
T_{CE} = &\ (B_{pn}\sin\varepsilon - B_{nq}\cos\varepsilon)\dot{\omega}_{Az}\\
&- \frac{1}{2}[(B_q - B_p)\sin(2\varepsilon) + 2B_{pn}\cos(2\varepsilon)]\,\omega_{Az}^2,
\end{aligned} \tag{37}$$

where T_{BE} is the moment of inertia disturbance to the movement of the barrel. T_{CE} is the moment of disturbance caused by the interaction between the axes.

2.3. Calculating the rotation angle of the barrel and turret for a given set of target coordinates in space

The model calculates the angles γ and ε when the target has coordinates (X_0, Y_0, Z_0) in space described in the inertial coordinate system. Transform the inertial coordinate system to the coordinate system of the barrel and turret along with the displacement of the vehicle body z when the vehicle moves on the road.

The total rotation matrix from the inertial system to the system of the vehicle body is as follows:

$$R = R_{z(\psi)}R_{y(\theta_E)}R_{x(\varphi_E)}. \tag{38}$$

The rotation matrix around the x (roll), y (pitch),

Road surface			
V	$8.33\,\mathrm{m\,s^{-1}}$	q_{0T}, q_{0P}	$0.01\,\mathrm{m}$
L	$2.8\,\mathrm{m}$	S_{0T}, S_{0P}	$4\,\mathrm{m}$
Front axle			
m_1	$210\,\mathrm{kg}$	K_{L1T}, K_{L1P}	$8\times10^5\,\mathrm{N\,m^{-1}}$
b	$0.75\,\mathrm{m}$	C_{L1T}, C_{L1P}	$2\times10^3\,\mathrm{N\,s\,m^{-1}}$
Rear axle			
m_2	$260\,\mathrm{kg}$	K_{L2T}, K_{L2P}	$8\times10^5\,\mathrm{N\,m^{-1}}$
C_{L2T}	$8\times10^5\,\mathrm{N\,s\,m^{-1}}$	C_{L2P}	$8\times10^5\,\mathrm{N\,s\,m^{-1}}$
Vehicle body			
M	$4\,180\,\mathrm{kg}$	K_{1T}, K_{1P}	$18\times10^4\,\mathrm{N\,m^{-1}}$
a_1	$1.3\,\mathrm{m}$	K_{2T}, K_{2P}	$18\times10^4\,\mathrm{N\,m^{-1}}$
a_2	$1.5\,\mathrm{m}$	C_{1T}, C_{1P}	$2\times10^3\,\mathrm{N\,s\,m^{-1}}$
c	$0.6\,\mathrm{m}$	C_{2T}, C_{2P}	$2\times10^3\,\mathrm{N\,s\,m^{-1}}$

TABLE 1. Parameters of the road surface and the UGV.

and z (yaw) axes is as follows:

$$R_{x(\varphi_E)}=\begin{bmatrix}1&0&0\\0&\cos\varphi_E&-\sin\varphi_E\\0&\sin\varphi_E&\cos\varphi_E\end{bmatrix},$$
$$R_{y(\theta_E)}=\begin{bmatrix}\cos\theta_E&0&\sin\theta_E\\0&1&0\\-\sin\theta_E&0&\cos\theta_E\end{bmatrix},\qquad(39)$$
$$R_{z(\psi)}=\begin{bmatrix}\cos\psi&-\sin\psi&0\\\sin\psi&\cos\psi&0\\0&0&1\end{bmatrix}.$$

Then, we can calculate the matrix R and its inverse matrix R^{-1} as follows:

$$R=\begin{bmatrix}\cos\theta_E\cos\psi&\sin\varphi_E\sin\theta_E\cos\psi-\cos\varphi_E\sin\psi&\dots\\\cos\theta_E\sin\psi&\cos\varphi_E\cos\psi+\sin\varphi_E\sin\theta_E\sin\psi&\dots\\-\sin\psi&\cos\theta_E\sin\varphi_E&\dots\\&\dots&\cos\varphi_E\sin\theta_E\cos\psi+\sin\varphi_E\sin\psi\\&\dots&\cos\varphi_E\sin\theta_E\sin\psi-\sin\varphi_E\cos\psi\\&\dots&\cos\theta_E\cos\varphi_E\end{bmatrix},$$
$$R^{-1}=\begin{bmatrix}\cos\theta_E\cos\psi&\dots\\\sin\varphi_E\sin\theta_E\cos\psi-\cos\varphi_E\sin\psi&\dots\\\cos\varphi_E\sin\theta_E\cos\psi+\sin\varphi_E\sin\psi&\dots\\\dots&\cos\theta_E\sin\psi&\dots\\\dots&\cos\varphi_E\cos\psi+\sin\varphi_E\sin\theta_E\sin\psi&\dots\\\dots&\cos\varphi_E\sin\theta_E\sin\psi-\sin\varphi_E\cos\psi&\dots\\&&-\sin\psi\\&&\cos\theta_E\sin\varphi_E\\&&\cos\theta_E\cos\varphi_E\end{bmatrix}.\qquad(40)$$

The target coordinates in the vehicle body system can be calculated as follows:

$$\begin{bmatrix}x_t\\y_t\\z_t\end{bmatrix}=R^{-1}\begin{bmatrix}X_0\\Y_0\\Z_0-z\end{bmatrix}$$
$$=\begin{bmatrix}\cos\theta_E\cos\psi&\dots\\\sin\varphi_E\sin\theta_E\cos\psi-\cos\varphi_E\sin\psi&\dots\\\cos\varphi_E\sin\theta_E\cos\psi+\sin\varphi_E\sin\psi&\dots\\\dots&\cos\theta_E\sin\psi&\dots\\\dots&\cos\varphi_E\cos\psi+\sin\varphi_E\sin\theta_E\sin\psi&\dots\\\dots&\cos\varphi_E\sin\theta_E\sin\psi-\sin\varphi_E\cos\psi&\dots\\&\dots&-\sin\psi\\&\dots&\cos\theta_E\sin\varphi_E\\&\dots&\cos\theta_E\cos\varphi_E\end{bmatrix}\begin{bmatrix}X_0\\Y_0\\Z_0-z\end{bmatrix}\qquad(41)$$
$$=\begin{bmatrix}X_0\cos\theta_E\cos\psi\\X_0\left(\sin\varphi_E\sin\theta_E\cos\psi-\cos\varphi_E\sin\psi\right)\\X_0\left(\cos\varphi_E\sin\theta_E\cos\psi+\sin\varphi_E\sin\psi\right)\\+Y_0\cos\theta_E\sin\psi\\+Y_0\left(\cos\varphi_E\cos\psi+\sin\varphi_E\sin\theta_E\sin\psi\right)\\+Y_0\left(\cos\varphi_E\sin\theta_E\sin\psi-\sin\varphi_E\cos\psi\right)\\-\left(Z_0-z\right)\sin\psi\\+\left(Z_0-z\right)\cos\theta_E\sin\varphi_E\\+\left(Z_0-z\right)\cos\theta_E\cos\varphi_E\end{bmatrix}.$$

Finally, the barrel and turret rotation angle can be calculated as follows:

$$\gamma=\tan^{-1}\left(\frac{y_t}{x_t}\right),\quad\varepsilon=\tan^{-1}\left(\frac{z_t}{\sqrt{x_t^2+y_t^2}}\right).\qquad(42)$$

3. Simulation using MATLAB-Simulink software

3.1. Input parameters

This paper presents a simulation model of a UGV travelling in a straight line at a constant speed, neglecting angular oscillations about the vertical axis. The input parameters for simulating the unmanned vehicle and the weapon system, along with the target coordinates, are presented in Tables 1 and 2 [1, 2, 6, 10, 15–17].

Turret	[kg m^2]	Barrel	[kg m^2]	Target	[m]
A_m	2 586	B_p	223	X_0	270
A_n	2 443	B_n	253		
A_z	2 398	B_q	105	Y_0	350
A_{mn}	486.4	B_{pn}	45.6		
A_{mz}	495.3	B_{pq}	53.2	Z_0	300
A_{nz}	387.4	B_{nq}	45.4		

TABLE 2. Parameters of the moments of inertia and target coordinates.

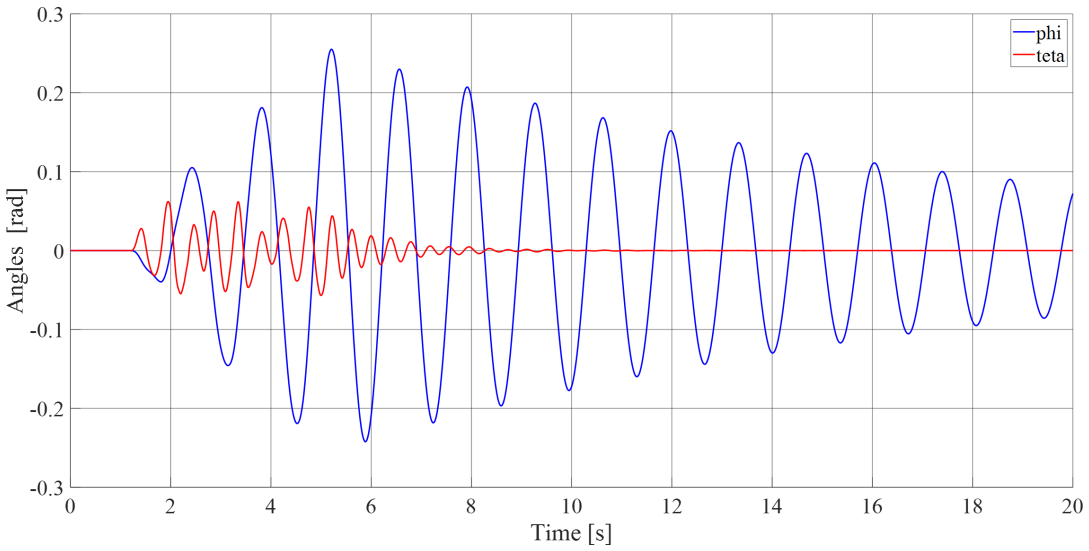

FIGURE 4. Vibration plots of the vehicle body roll and pitch angles.

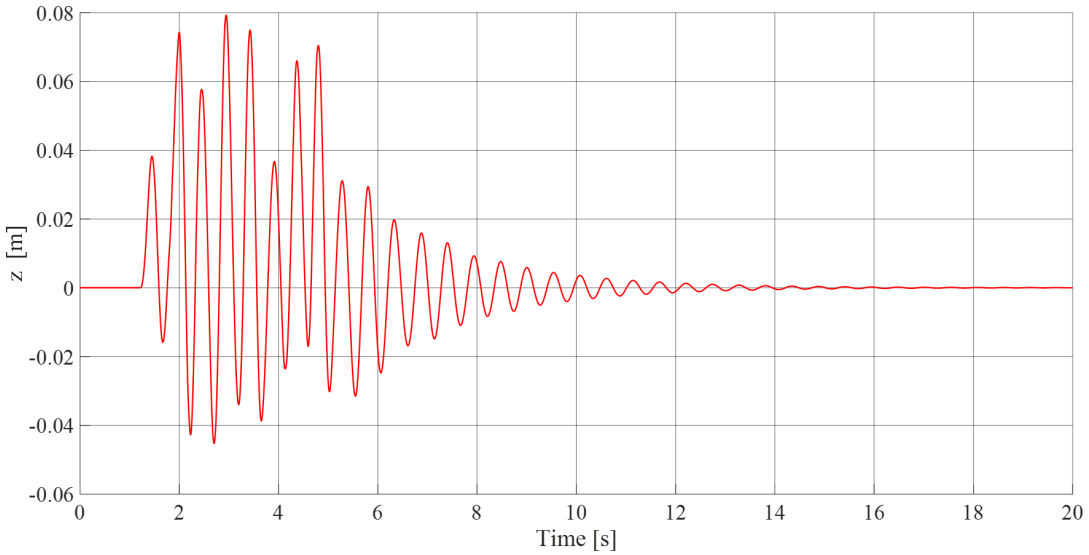

FIGURE 5. Vertical displacement vibration at the centre of mass of the vehicle body.

3.2. SIMULATION RESULTS FOR THE VEHICLE BODY

Figures 4 and 5 show the simulation results of the roll and pitch angles, as well as the vertical displacement of the vehicle body.

As can be seen from graph in Figure 4, both the roll and pitch angles exhibit damped oscillatory behaviour over time. This reflects the dynamic response characteristics of the suspension system as the vehicle traverses uneven terrain. The roll angle shows a large amplitude, reaching a peak of approximately ± 0.25 rad during the initial phase. It then gradually decreases and approaches a steady state. Roll vibrations have a relatively regular period and a longer decay time, indicating a strong influence from the asymmetric excitation between the left and right sides of the road. This also suggests that the suspension system has a limited capacity to absorb lateral vibrations.

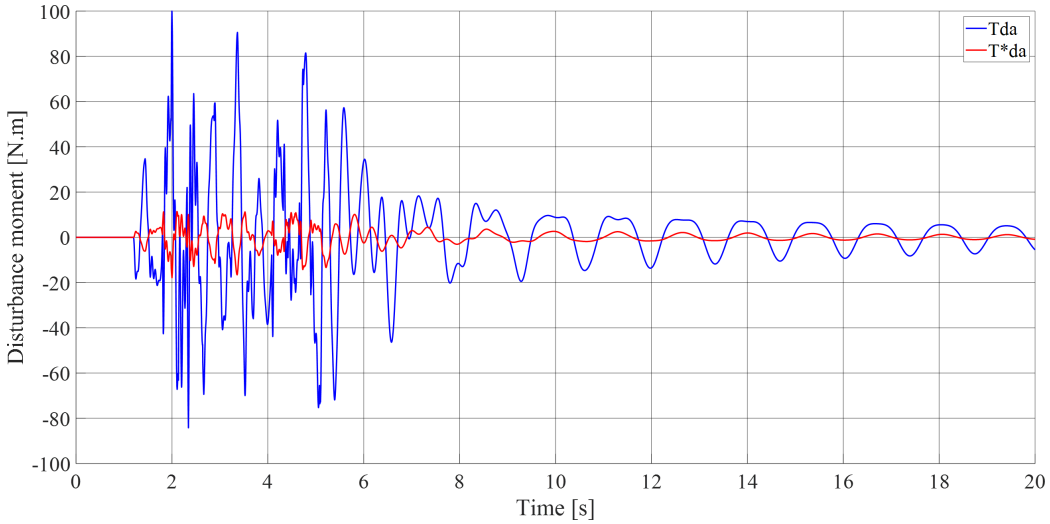

Figure 6. The disturbance torque components acting on the azimuth motion.

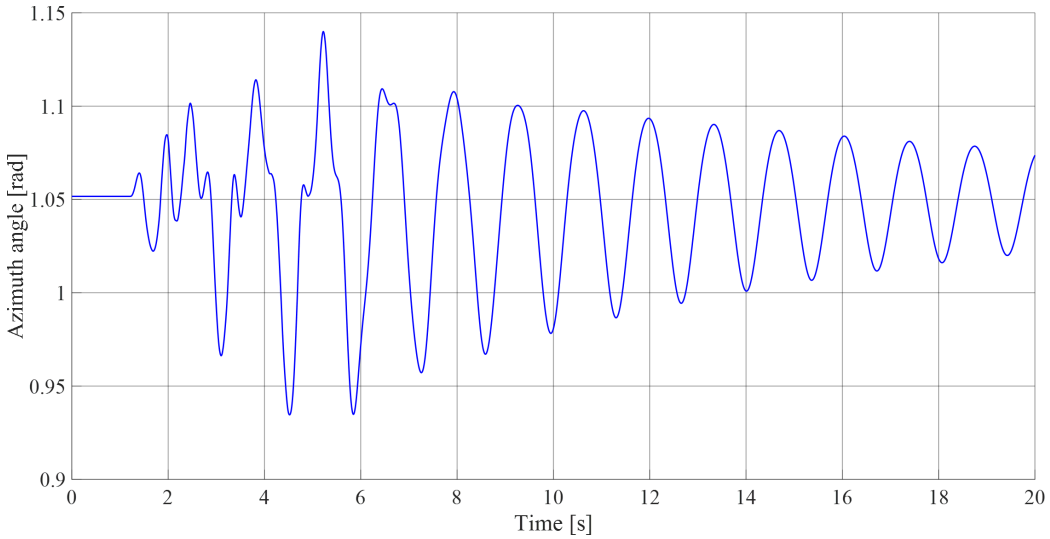

Figure 7. The vibration graph of the azimuth rotation angle in the horizontal plane.

In contrast, the pitch angle fluctuates within ±0.05 rad and damps more quickly. Pitch oscillations primarily occur in the early phase when the vehicle encounters unevenness, decaying rapidly towards near-equilibrium values. These observations demonstrate that the front-rear suspension system effectively reduces longitudinal vibrations. At the same time, road-induced excitation in the longitudinal direction is less pronounced than asymmetric lateral excitation. The significant differences in amplitude and damping between φ and θ indicate that lateral oscillation is the dominant vibration component of the vehicle body travelling on asymmetric uneven terrain. This is an important consideration for designing stabilisation systems and aiming control for weapon systems.

Figure 5 shows the vertical displacement of the vehicle's centre of gravity, which clearly exhibits damped vibrations. The initial amplitude is relatively large, reaching about ±0.075 m within the first 2–3 seconds. This reflects strong excitation from the uneven road surface. The amplitude decreases and stabilises near equilibrium after approximately 2–5 seconds, indicating that the suspension system effectively absorbs energy. The oscillations are quasi-periodic, with damping characteristics typical of lightly damped mechanical systems. Overall, the suspension system successfully reduces vertical vibrations, although the initial response remains significant due to road impacts. This highlights the critical role of suspension design in controlling vertical movement of the vehicle body travelling on rough terrain.

3.3. Simulation results for the azimuth dynamics

The time histories of the turret's angular vibrations and the corresponding disturbance torques are presented in Figures 6 and 7. These figures illustrate how the system responds to road-induced excitations, highlighting the characteristics of both the overall and secondary disturbance components acting on the azimuth axis.

The graph in Figure 6 illustrates the two components of disturbance torque, T_{da} and T_{da}^{*}, varying over time during the movement of the unmanned vehicle. These disturbances become apparent after the first second, reflecting the moment when the system begins to be affected by road surface irregularities. During the strong excitation phase from seconds 1 to 7, the amplitude of T_{da} oscillates extremely violently, with peak values reaching approximately 90 Nm and troughs falling below −80 Nm. This complex and unstable variation indicates the direct and severe impact of terrain shocks on the azimuth axis of the stabilisation platform.

After the 7 seconds, the system gradually enters a stabilisation phase, with disturbance amplitudes beginning to decrease and transition into harmonic oscillations, maintaining an amplitude around 10 Nm. When comparing the two components, T_{da} exhibits overall disturbance characteristics with large variations in amplitude and frequency, whereas T_{da} shows significantly lower amplitudes, frequently remaining below 10 Nm. This suggests that T_{da} may represent a secondary disturbance component or has been partially mitigated by the mechanical structure of the system. The fact that the oscillations continue up to the 20^{th} second without fully decaying to zero confirms that the stabilisation platform always operates in an environment with persistent disturbances. In order to maintain line-of-sight accuracy, the controller must be capable of responding extremely rapidly to compensate for the large disturbance torque peaks that occur during the initial phase of operation.

In Figure 7, the graph of azimuth angular vibrations in the horizontal plane illustrates the direct influence of dynamic excitations from the road on the weapon system. During the first second, when the vehicle moves on a flat surface, the azimuth angle remains stable at a set value of 1.05 rad, corresponding to the initial target orientation relative to the vehicle's direction of motion. However, as soon as the vehicle enters the rough road section (from seconds 1 to 7), the system becomes severely unstable due to shocks transmitted from the road through the suspension and vehicle body. During this phase, the azimuth angle oscillates violently with a large amplitude, reaching a maximum of 1.14 rad and a minimum of 0.93 rad. This unstable variation reflects the damped oscillation characteristics of a mechanical system under the influence of dynamic disturbance torques.

After the strong excitation phase, from the 7^{th} second onwards, the vibration amplitude gradually decreases and transitions into harmonic oscillations around the equilibrium position, indicating the partial self-stabilising capability of the mechanical structure. Although the amplitude diminishes, the fact that the oscillations persist until the 20^{th} second without fully decaying highlights the significant challenges involved in maintaining line-of-sight accuracy. These results confirm that, without the intervention of advanced disturbance-compensating controllers, such angular deviations would significantly reduce the probability of hitting the target when the vehicle is operating in complex terrain conditions.

3.4. Simulation results for the elevation dynamics

The graphs of the kinematic perturbation moment components and the barrel rotation angle are given in Figures 8 and 9.

The graph in Figure 8 depicts the components of dynamic disturbance torques acting on the barrel motion in the vertical plane, including the inertial disturbance torque T_{BE} and the cross-axis interaction torque T_{CE}. During the initial phase, when the vehicle travels on a flat road surface (0–1 s), the disturbance torques remain approximately zero before beginning to oscillate strongly once the vehicle enters a road section with surface irregularities after the first second.

As can be seen from the time-history observation, the T_{CE} component plays a dominant role, exhibiting very large oscillation amplitudes during the strong excitation phase (from 1 to approximately 7 seconds), with peak values reaching approximately 60 Nm and troughs decreasing to −38 Nm. This behaviour indicates that the cross-axis interaction between the turret and the barrel generates significant impulse forces, leading to severe instability of the system. In contrast, the inertial disturbance torque T_{CE} has a much smaller amplitude, oscillating within a narrow range from −10 Nm to 20 Nm. At certain instants, the in-phase combination of T_{BE} and T_{CE} further amplifies the overall disturbance torque acting on the barrel. After the 8^{th} second, both components transition into damped harmonic oscillations with rapidly decreasing amplitudes, gradually approaching a steady state as the energy from the road-induced shocks is dissipated by the suspension system. These results emphasise the critical importance of compensating for the cross-axis disturbance component TCE in order to maintain line-of-sight accuracy under real operating conditions.

Figure 9 shows the graph of the barrel's angular vibrations in the vertical plane and illustrates the dynamic response of the weapon system to disturbance torques when the unmanned vehicle moves over complex terrain. These vibrations reach a maximum of approximately 0.79 rad and a minimum of 0.38 rad, fluctuating around the initial reference value. This variation indicates that the barrel is significantly affected by both the cross-axis interaction torques and the inertial disturbance torques transmitted from the vehicle body motion. Although the vibration amplitude gradually decreases after the 10^{th} second, the vibration frequency remains high and persists continuously until the 20^{th} second. The fact that the barrel elevation angle cannot quickly return to the equilibrium state highlights the risk of line-of-sight degradation. These simulation results emphasise the need to implement advanced control strategies to com-

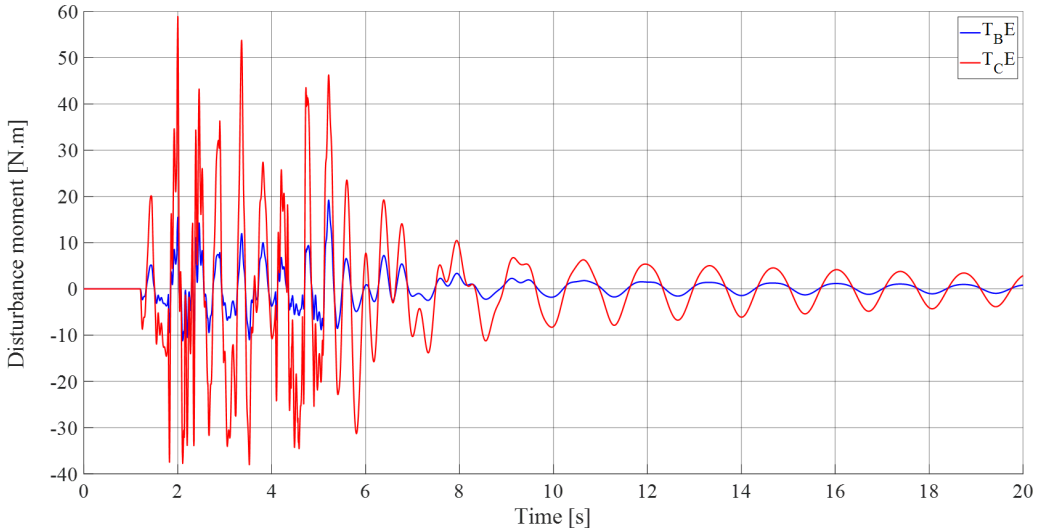

Figure 8. Moment diagram of the turbulence components acting on the barrel.

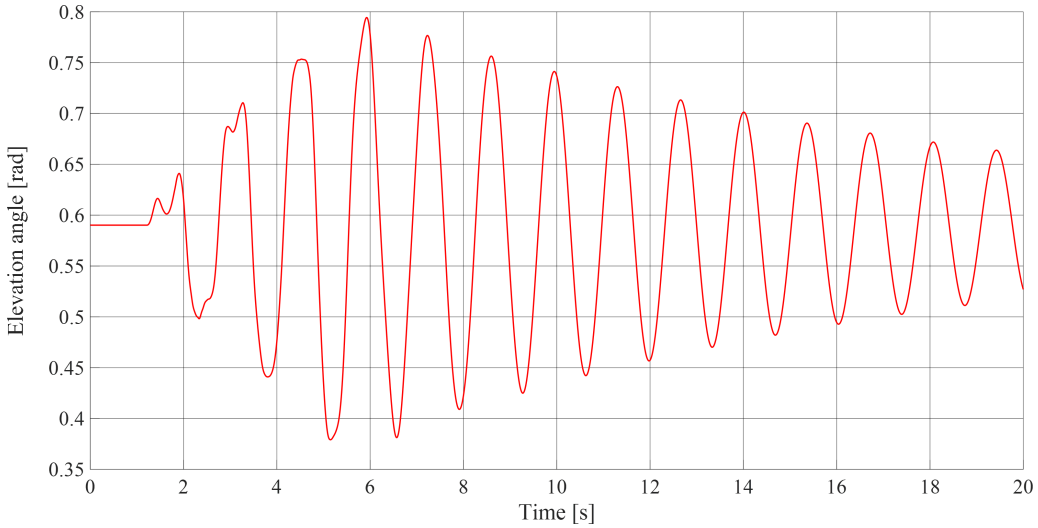

Figure 9. Angular vibration graph of the barrel in the vertical plane.

pensate for angular deviations in real time, ensuring accurate target tracking of the weapon system on the UGV.

4. Experimental measurement of the vibrations of an UGV body

4.1. Experimental model

To verify the dynamic characteristics of the suspension system and the influence of the road profile in real-world conditions, a small-scale experiment was conducted to measure the vehicle's vibrations while travelling over uneven surfaces. The UGV model used in the experiment is a four-wheeled platform with a dependent suspension system, equipped with a laser device mounted on top of the vehicle body to measure vibrations. Figure 10 illustrates the detailed structure of the experimental model, in which the vehicle is set to move at a constant speed along a predefined route.

The small-scale UGV model has a mass of 80 kg, measures $1.1 \times 0.7 \times 0.6$ m, and has a wheel diameter of 0.3 m. In this experimental setup, a laser source is fixed on the vehicle frame, projecting a light spot onto a flat wall surface parallel to the vehicle's direction of motion. A high-speed camera (265 frames s^{-1}) is mounted on a fixed tripod in a position opposite the wall, ensuring full coverage of the laser spot trajectory on the wall as the vehicle operates.

The experimental procedure consists of the following main steps (Figure 11) [11, 14]:

- Trajectory setup: The unmanned vehicle is driven at a constant speed over an uneven surface to excite vibrations in the suspension system.
- Data recording: The entire movement of the laser spot on the wall is captured by the high-speed camera; any vibrations of the vehicle body are reflected by changes in the position of the laser spot.
- Image processing: The acquired video is processed using specialised image analysis software to track the centroid of the laser spot in each frame.

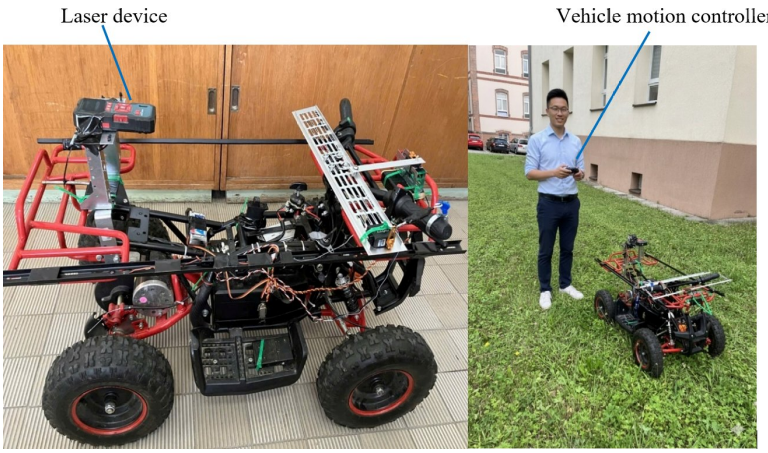

FIGURE 10. UGV model used in the experiment.

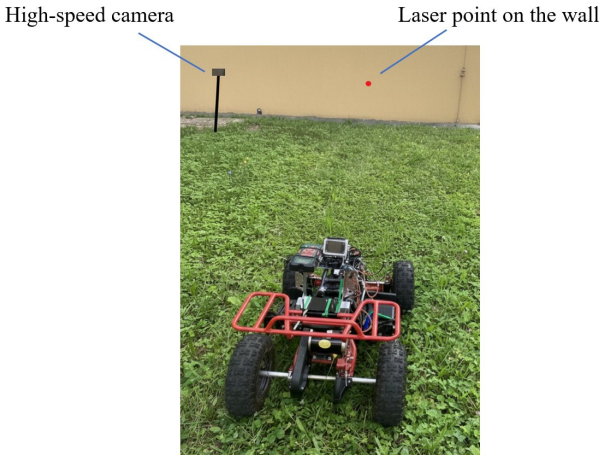

FIGURE 11. The position of the camera and the laser point on the wall.

- Graph extraction: From the pixel position data of the laser spot over time, the algorithm converts the measurements into physical units to reconstruct the vehicle body's vibration graphs in the corresponding planes.

The experiment was conducted using two different terrain simulation scenarios:

- Vehicle traveling on uneven terrain (Random terrain): This experiment aimed to assess the stability of the vehicle system under continuous random disturbances, simulating real-world operating conditions of natural terrain.
- Vehicle passing over a symmetric bump (Symmetric bump): The vehicle traversed a single rectangular bump with a height of 10 cm and a width of 20 cm, spanning the full width of the vehicle and simultaneously affecting both wheels on the same axle. This experiment focused on analysing the vehicle's transient response and the vibration damping capability of the vehicle body under sudden excitation.

Conducting both scenarios allowed the research team to evaluate the influence of different road conditions on the weapon system.

4.2. Experimental results

4.2.1. Experimental results on a random road surface

In Figure 12, the oscillation plot in the horizontal plane reflects the directional instability and the lateral yawing phenomenon of the vehicle when operating on real terrain. The experimental results show that although the vehicle moves along a straight trajectory, the asymmetric excitations from the road surface still generate small oscillations with continuously varying amplitudes. Peak impulses in the plot coincide with the moments when the wheels encounter surface irregularities, producing a yawing moment about the vertical axis of the vehicle body. Although the amplitude of horizontal oscillations is lower than that of the vertical oscillations, they are the primary cause of azimuth angle errors in the camera/weapon system, thereby necessitating a stabilised platform controller to suppress these disturbances and ensure a fixed line of sight on the target. The vibration plot in the vertical plane in Figure 13 provides an intuitive insight into the shock absorption capability of the suspension system when the vehicle encounters an obstacle. From the data, it can be observed that the displacement amplitude dy varies significantly at the moment of contact with the bump, reflecting the continuous compression and rebound processes of the damping components. A notable characteristic is the appearance of secondary oscillation bands following the primary impulse, indicating the dynamic response of the vehicle body before returning to a state of dynamic equilibrium. The analysis of peak-to-peak amplitudes and oscillation decay rates in this plot constitutes an important basis for evaluating the stiffness and damping coefficients of the experimental model. These results also confirm that vertical disturbances are the dominant source of excitation leading to instability in equipment mounted on the vehicle. Figure 14 shows the plot of the laser spot position on the wall, which serves as a combined result, reflecting the relative displacement of the system in observable real space. Unlike intrinsic sensor measurements, this plot directly records the

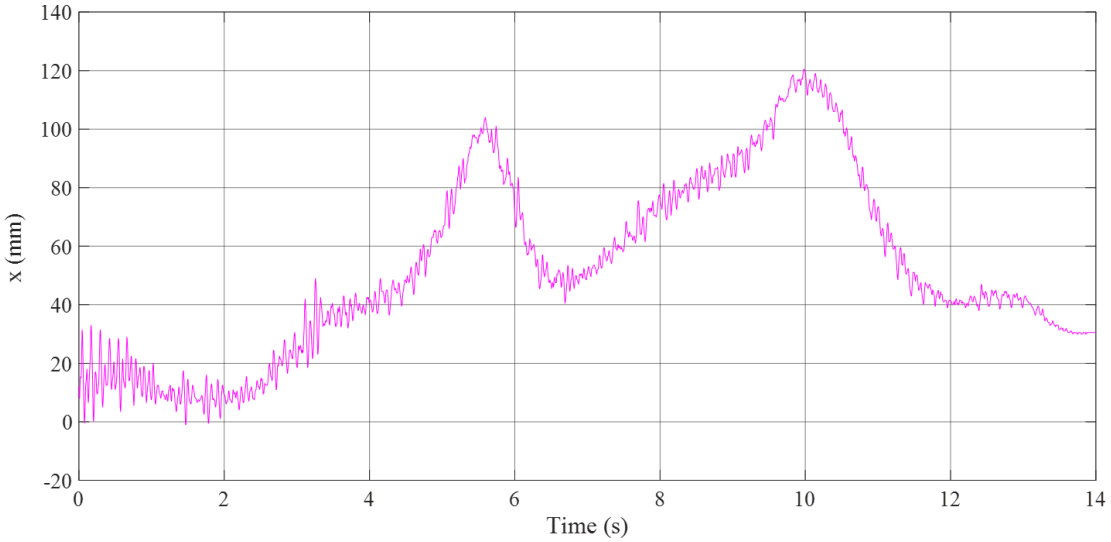

Figure 12. Vibration of the vehicle in the horizontal plane under random road surface conditions.

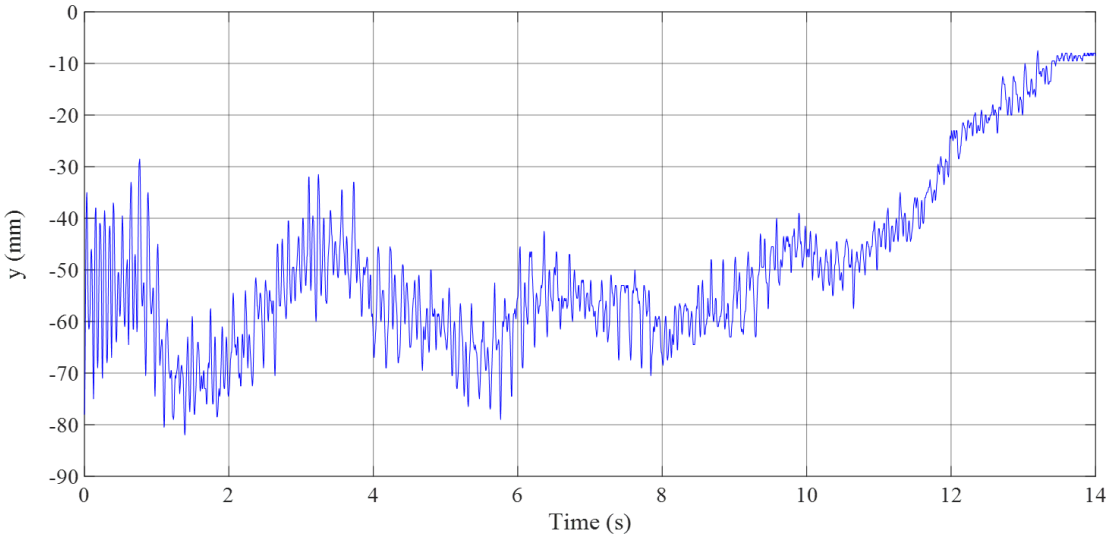

Figure 13. Vibration of the vehicle in the vertical plane under random road surface conditions.

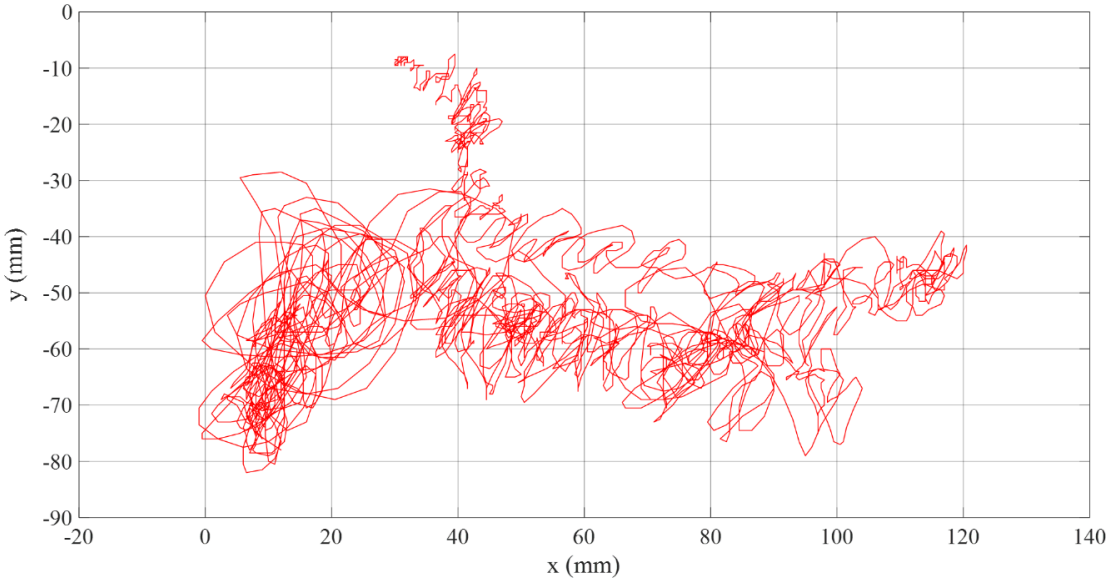

Figure 14. Position of the laser on the wall under random road surface conditions.

trajectory of the light spot, illustrating the amplification of vehicle body oscillations proportional to the distance from the emission source to the wall surface. Variations in the laser coordinates on the wall plane not only demonstrate vertical vibrations but also reveal small angular deviations, causing the laser spot to form complex trajectories rather than an ideal straight line. Analysing this plot enables the laser error disk to be identified accurately, thereby providing practical input data for tuning error compensation parameters in the camera observation system and stabilising the line of sight under dynamic experimental conditions.

4.2.2. Experimental results for a single-bump road surface

Figures 15 and 16 show that when the vehicle traverses a single bump, the oscillations in the vertical and horizontal planes exhibit different dynamic characteristics while remaining closely coupled. Vertical oscillations play a dominant role, with large amplitudes and immediate responses upon the contact with the obstacle, directly reflecting the changes in road elevation. In contrast, horizontal oscillations have smaller amplitudes and arise from traction imbalance and vehicle body inertia, leading to lateral sway and slight directional deviations. The combination of strong vertical impulses and complex horizontal disturbances results in a complex spatial motion trajectory, underscoring the importance of multi-axis stabilisation in maintaining the accuracy of vehicle-mounted equipment. The simultaneous variations along both the X and Y axes in the plot shown in Figure 17 demonstrate that when the vehicle passes over a bump, the system experiences not only vertical bouncing but also lateral sway, resulting in target tracking errors along both axes. These experimental data provide important real-world evidence for validating the line-of-sight stabilisation performance of the controller under practical operating conditions.

5. Discussion

From the system of mathematical equations and simulation results, it is evident that dynamic disturbances significantly affect the weapon system of a UGV during operation. Vibrations originating from the drivetrain and natural oscillations of the vehicle structure, particularly when traversing uneven terrain, generate complex mechanical vibrations transmitted to the weapon system. Random impact forces from the ground, such as wheels encountering obstacles or depressions, produce large impulses over short durations, affecting stability and orientation. Changes in dynamic loads during sudden manoeuvres, including acceleration, braking, or sharp turns, further alter the force distribution on the weapon system. Additionally, interactions between mechanical components, including joint play, suspension response, and manufacturing or assembly imperfections act as continuous disturbance sources. The operation of control motors, which generate the torque for the turret and gun barrel movement, also contributes to instability.

These dynamic disturbances have a direct and profound impact on the weapon system's aiming performance. Continuous mechanical oscillations and background vibrations reduce stability, causing the aiming angle to deviate from its desired value. Even small-amplitude oscillations can compromise the high precision required for maintaining the line of sight, especially when targeting small or long-range objects. Instantaneous impulses from terrain impacts induce sudden fluctuations in weapon position and orientation, which can result in projectiles missing their target, particularly if they occur during aiming or firing. In complex operational environments that require rapid reaction times, these disturbances prolong stabilisation and delay firing readiness, thereby reducing overall combat performance.

Moreover, dynamic load variations caused by vehicle manoeuvres induce rapid changes in the tilt and azimuth angles of the weapon system. Without timely and precise compensation, the aiming system cannot maintain a stable line of sight, leading to increased projectile dispersion and reduced target engagement probability. This highlights the critical importance of robust stabilisation and control mechanisms for UGV-mounted weapon systems.

Compared to prior studies, this work extends the understanding of disturbance effects by considering the influence of road profile irregularities on UGV weapon systems. Previous research [1, 2] focused primarily on the kinematic modelling of two-axis gimbal systems (yaw-pitch) and derived equations of motion using moment or Lagrange methods to analyse inertia, disturbances, and axis interactions. Subsequent studies [3–5] developed cascade and fuzzy PID control strategies to stabilise the line of sight under and compensate for external disturbances, demonstrating improvements in gimbal performance and aiming accuracy. In [6], the authors investigated turret and barrel control for main battle tanks, focusing mainly on modelling and control of vehicle-mounted weapon systems.

This study goes beyond these earlier works by incorporating asymmetric, alternating bump profiles as part of the road surface, providing a realistic source of external disturbance that combines vertical impulses and lateral oscillations. Small-scale experiments were conducted to measure UGV oscillations over both a single bump and a random road surface, validating the simulation results. These experiments confirm that uneven road profiles, even with minor asymmetries, can generate significant dynamic disturbances that affect the stability and aiming accuracy of the weapon system, highlighting the necessity of multi-axis stabilisation and controller tuning for practical operations.

In summary, the results demonstrate that the combination of vertical and lateral dynamic disturbances, amplified by an irregular road surface, produces com-

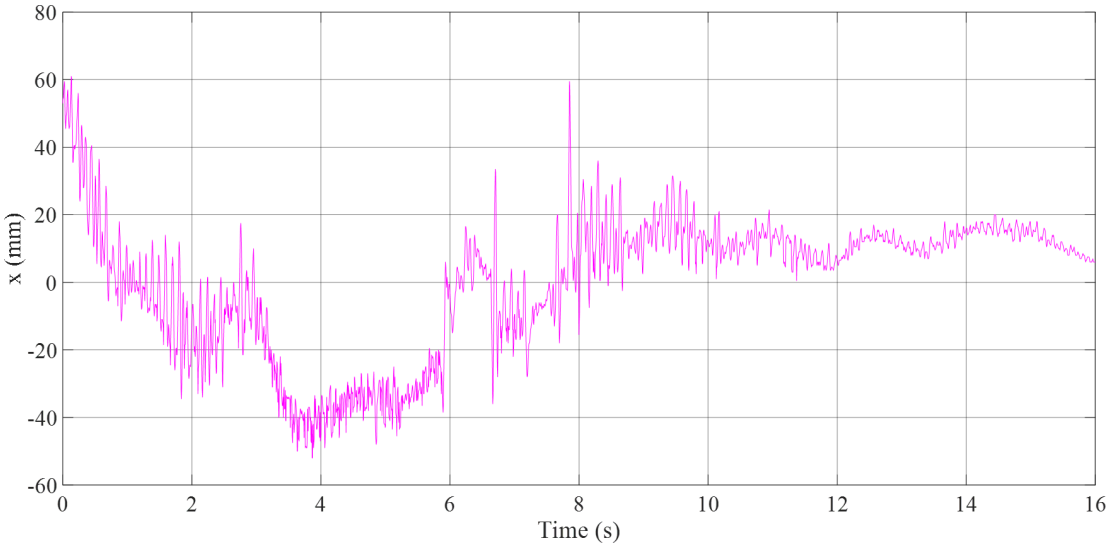

FIGURE 15. Vibration of the vehicle in the horizontal plane under single-bump road conditions.

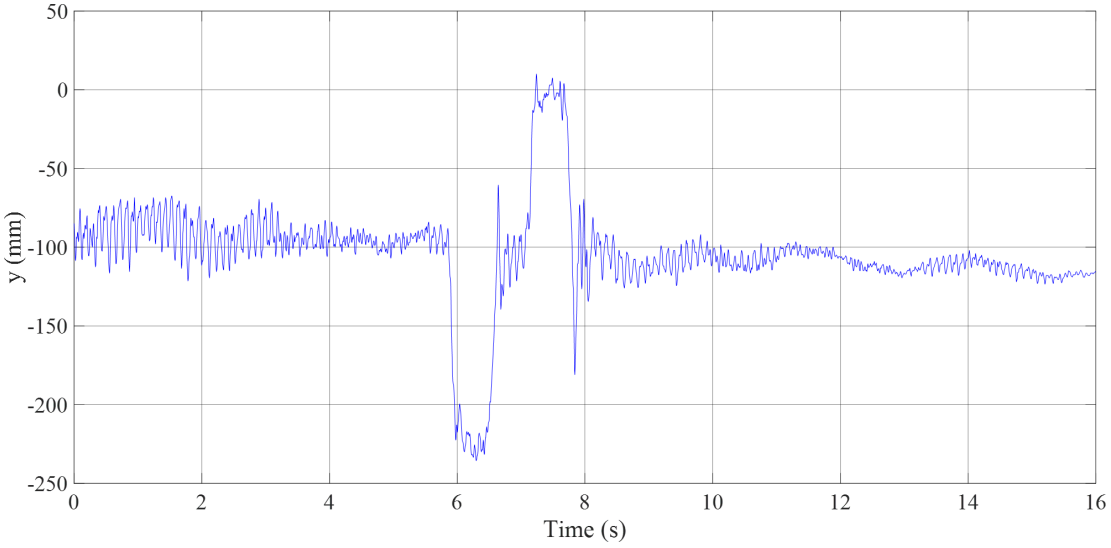

FIGURE 16. Vibration of the vehicle in the vertical plane under single-bump road conditions.

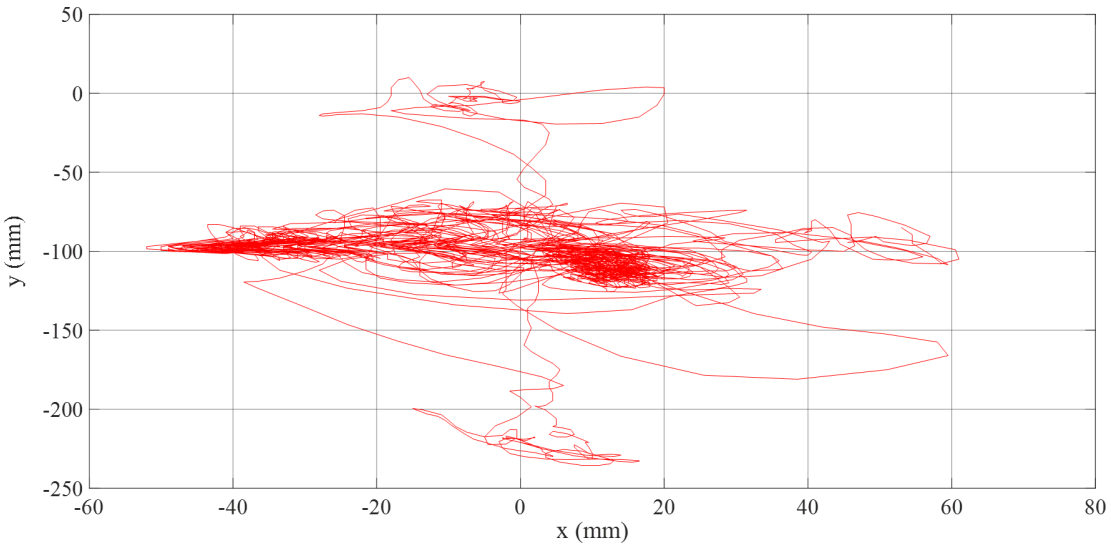

FIGURE 17. Position of the laser on the wall under single-bump road conditions.

plex motion trajectories for the weapon system. This work bridges the gap between previous gimbal-focused studies and real-world conditions, emphasising the practical impact of terrain-induced disturbances on the performance of UGV-mounted weapons, and provides critical experimental data to guide controller design and stabilisation strategies.

6. Conclusion

This study investigated the influence of dynamic disturbances on the accuracy of weapon systems mounted on UGVs in uneven terrain conditions. The research had three main objectives:

- To develop a comprehensive mathematical model describing dynamic disturbances caused by mass imbalances and cross-inertial effects in UGV-weapon systems. This objective was achieved by formulating nonlinear dynamic equations using Euler rotation matrices and coordinate transformation methods, incorporating suspension-induced disturbances. The model effectively captures the influence of cross-inertial interactions between the turret and gun barrel on the behaviour of the system.
- To analyse the impact of asymmetrical and non-uniform road surfaces on weapon system vibrations. This was achieved by introducing road profiles featuring alternating bumps, semi-sinusoidal, trapezoidal, and rectangular ridge shapes to reflect battlefield-like terrain. The simulation results showed that asymmetrical road excitation significantly amplifies both vertical and lateral disturbances, leading to increased angular deviations and instability of the aiming system.
- To validate the simulation model with experimental measurements. A scaled UGV model was tested on a single bump and a random rough road section, measuring the oscillations of the vehicle body. The experimental data confirmed the trends predicted by the simulation, showing that terrain-induced vibrations and suspension dynamics significantly affect the stability of the weapon system.

The study demonstrated that dynamic disturbances, even with small amplitudes, can substantially reduce aiming precision. The developed modelling approach provides a quantitative basis for calculating compensation angles and predicting weapon system behaviour in realistic operating conditions. Furthermore, the results highlight the necessity of multi-axis stabilisation and advanced control strategies to mitigate disturbances, enhance aiming stability, and improve firing accuracy.

Future work will focus on implementing adaptive or intelligent controllers, such as fuzzy-PID or model predictive control, and validating their effectiveness through hardware experiments. Expanding the model to include environmental uncertainties and real-time sensor feedback will further strengthen the reliability of stabilisation systems for UGV-mounted weapons in complex combat scenarios.

List of symbols

q_{0T}, q_{0P} The height of the bumps on the road surface on the left and right, respectively [m]

S_{0T}, S_{0P} Wavelength of the road surface on the left and right [m]

$K_{L1T}, K_{L1P}, K_{L2T}, K_{L2P}$ Elasticity coefficient of the front and rear tyres, left and right, respectively [$\mathrm{N\,m^{-1}}$]

$C_{L1T}, C_{L1P}, C_{L2T}, C_{L2P}$ Damping coefficient of the front and rear tyres, left and right, respectively [$\mathrm{N\,s\,m^{-1}}$]

$K_{1T}, K_{1P}, K_{2T}, K_{2P}$ Elasticity coefficient of the front and rear suspension, left and right, respectively [$\mathrm{N\,m^{-1}}$]

$C_{1T}, C_{1P}, C_{2T}, C_{2P}$ Damping coefficient of the front and rear suspension, left and right, respectively [$\mathrm{N\,s\,m^{-1}}$]

a_1, a_2 Distance from the centre of gravity of the vehicle body to the front and rear axles, respectively [m]

$2b$ Average distance between the right and left wheel tracks [m]

$2c$ Average distance between the right and left suspension [m]

Z_{01}, Z_{02} Vertical displacement of the front and rear axles, respectively [m]

φ_1, φ_2 Roll angle of the front and rear axles, respectively [rad]

Z_0 Vertical displacement of the body of the vehicle [m]

φ, θ Roll and pitch angles of the body of the vehicle, respectively [rad]

L_n Barrel length [m]

V Vehicle speed [$\mathrm{m\,s^{-1}}$]

$F_{KL1T}, F_{KL1P}, F_{KL2T}, F_{KL2P}$ Elastic force of the front and rear tires, left and right, respectively [N]

$F_{CL1T}, F_{CL1P}, F_{CL2T}, F_{CL2P}$ Damping force of the front and rear tires, left and right, respectively [N]

$F_{L1T}, F_{L1P}, F_{L2T}, F_{L2P}$ Elastic force of the front and rear suspension, left and right, respectively [N]

$F_{C1T}, F_{C1P}, F_{C2T}, F_{C2P}$ Damping force of the front and rear suspension, left and right, respectively [N]

m_1, m_2 Mass of the front and rear axles, respectively [kg]

J_{m1}, J_{m2} Mass moment of inertia of the front and rear axles, respectively [$\mathrm{kg\,m^2}$]

M Mass of the body of the vehicle [kg]

J_φ, J_θ The moment of inertia of the mass of the body of the vehicle with respect to the axle OX0 and OY0, respectively [$\mathrm{kg\,m^2}$]

A_m, A_n, A_z The moments of inertia of the turret around the axes m, n, and z, respectively [$\mathrm{kg\,m^2}$]

A_{mn}, A_{nz}, A_{mz} The products of the turret's moments of inertia, the dynamic linkage value between the axes m, n, and z, respectively [$\mathrm{kg\,m^2}$]

B_p, B_n, B_q The moments of inertia of the barrel around the axes p, n, and q, respectively [$\mathrm{kg\,m^2}$]

B_{pn}, B_{pq}, B_{nq} The products of the barrel's moments of inertia, the dynamic linkage value between the axes p, n, and q, respectively [$\mathrm{kg\,m^2}$]

T_A The control torque acting on the turret [Nm]

T_E The control torque acting on the barrel [Nm]

Acknowledgements

This research was conducted at the Department of Weapons and Ammunition, University of Defence in Brno, and was supported by the Ministry of Defence of the Czech Republic through the project "Military Autonomous and Robotic Assets" VAROPS (DZRO-FVT22-VAROPS).

References

[1] S. Yoon, J. B. Lundberg. Equations of motion for a two-axes gimbal system. *IEEE Transactions on Aerospace and Electronic Systems* **37**(3):1083–1091, 2001. https://doi.org/10.1109/7.953259

[2] K. Fadaei, M. Ataei, S. Talebi. Modelling of a two-axis gimbal test-bed for line-of-sight stabilization. In I.Troch, F.Breitenecke (eds.), *Proceedings of the 5th International Conference on Mathematical Modelling – 5th MATHMOD Vienna*, pp. 8.1–8.10. 2006. [2025-09-25]. https://www.argesim.org/fileadmin/user_upload_argesim/ARGESIM_Publications_OA/MATHMOD_Publications_OA/MATHMOD_2006_AR30/Sessions/PHYS/360_P_Mohammad_Ataei.pdf

[3] M. Abdo, A. R. Toloei, A. R. Vali, M. R. Arvan. Cascade control system for two axes gimbal system with mass unbalance. *International Journal of Scientific & Engineering Research* **4**(9):903–912, 2013. [2025-09-25]. https://www.citefactor.org/article/index/5095/pdf/

[4] M. M. Abdo, A. R. Vali, A. R. Toloei, M. R. Arvan. Stabilization loop of a two axes gimbal system using self-tuning PID type fuzzy controller. *ISA Transactions* **53**(2):591–602, 2014. https://doi.org/10.1016/j.isatra.2013.12.008

[5] M. Abdo, A. R. Vali, A. R. Toloei, M. R. Arvan. Modeling, control and simulation of two axes gimbal seeker using fuzzy PID controller. In *Proceedings of the 22nd Iranian Conference on Electrical Engineering (ICEE)*, pp. 1342–1347. Tehran, Iran, 2014. https://doi.org/10.1109/IranianCEE.2014.6999742

[6] M. Lyth. *Modeling and evaluation of turret control systems for main battle tanks*. Master's thesis, KTH Royal Institute of Technology, School of Electrical Engineering and Computer Science, Stockholm, Sweden, 2021. [2025-09-25]. https://kth.diva-portal.org/smash/get/diva2:1637081/FULLTEXT01.pdf

[7] L. Wang, X. Tang, J. Fan, C. Huang. Prediction of firing accuracy of self-propelled antiaircraft gun in marching fire based on GA-BP neural network. *Journal of Physics: Conference Series* **2478**(9):092007, 2023. https://doi.org/10.1088/1742-6596/2478/9/092007

[8] Y. J. Kim, Y. Sohn, S. Chang, et al. Vibration control of car body and wheel motions for in-wheel motor vehicles using road type classification. *Actuators* **13**(2):80, 2024. https://doi.org/10.3390/act13020080

[9] O. Alexa, T. Ciobotaru, L. S. Grigore, et al. A review of mathematical models used to estimate wheeled and tracked unmanned ground vehicle kinematics and dynamics. *Mathematics* **11**(17):3735, 2023. https://doi.org/10.3390/math11173735

[10] B. V. Dung, M. Macko, Z. Krist, et al. Mathematical model of unmanned ground vehicle. In *Proceedings of the International Conference QUAERE*, pp. 765–771. Hradec Králové, Czech Republic, 2024. [2025-09-25]. http://www.vedeckekonference.cz/library/proceedings/quaere_2024.pdf

[11] V. D. Bui, M. Macko, D. D. Tran, et al. Research on vibrations of an unmanned vehicle on a random road surface. In *2025 International Conference on Military Technologies (ICMT)*, pp. 1–6. Brno, Czech Republic, 2025. https://doi.org/10.1109/ICMT65201.2025.11061271

[12] K. Chen, M. Zhang, X. Tong. Vibration characteristic analysis of vehicle air suspension based on fuzzy control. In *Proceedings of the 2nd International Conference on Electronic & Mechanical Engineering and Information Technology (EMEIT 2012)*, pp. 2196–2199. Paris, France, 2012. https://doi.org/10.2991/emeit.2012.486

[13] Z. Yin, R. Su, X. Ma. Dynamic responses of 8-DoF vehicle with active suspension: Fuzzy-PID control. *World Electric Vehicle Journal* **14**(9):249, 2023. https://doi.org/10.3390/wevj14090249

[14] V. D. Bui, M. Macko, D. B. Ngoc. Investigation of vehicle vibrations during traversal of speed bumps. *Advances in Military Technology* **20**(2):601–619, 2025. https://doi.org/10.3849/aimt.02031

[15] V. Šmilauer, J. Máca, M. Valášek. Dynamic bridge response for a bridge-friendly truck. *Acta Polytechnica* **44**(5–6):152–157, 2004. https://doi.org/10.14311/646

[16] A. M. Rad. Design and analysis of a fuzzy PID controller in comparison with other controllers for pitch-yaw gimbal. *Journal of Aerospace Science and Technology* **16**(1):1–15, 2023. https://doi.org/10.22034/jast.2023.377460.1140

[17] N. Ghaeminezhad, W. Daobo, F. Farooq. Stabilizing a gimbal platform using self-tuning fuzzy PID controller. *International Journal of Computer Applications* **93**(16):13–19, 2014. https://doi.org/10.5120/16298-6038